

Tailoring and Characterisation of Bioelectronic Interfaces

Aleksandr Markov

Schlüsseltechnologien / Key Technologies

Band / Volume 162

ISBN 978-3-95806-298-6

Forschungszentrum Jülich GmbH
Institute of Complex Systems
Bioelectronics (ICS-8)

Tailoring and Characterisation of Bioelectronic Interfaces

Aleksandr Markov

Schriften des Forschungszentrums Jülich
Reihe Schlüsseltechnologien / Key Technologies

Band / Volume 162

ISSN 1866-1807

ISBN 978-3-95806-298-6

Bibliografische Information der Deutschen Nationalbibliothek.
Die Deutsche Nationalbibliothek verzeichnet diese Publikation in der
Deutschen Nationalbibliografie; detaillierte Bibliografische Daten
sind im Internet über <http://dnb.d-nb.de> abrufbar.

Herausgeber und Vertrieb: Forschungszentrum Jülich GmbH
Zentralbibliothek, Verlag
52425 Jülich
Tel.: +49 2461 61-5368
Fax: +49 2461 61-6103
zb-publikation@fz-juelich.de
www.fz-juelich.de/zb

Umschlaggestaltung: Grafische Medien, Forschungszentrum Jülich GmbH

Druck: Grafische Medien, Forschungszentrum Jülich GmbH

Copyright: Forschungszentrum Jülich 2018

Schriften des Forschungszentrums Jülich
Reihe Schlüsseltechnologien / Key Technologies, Band / Volume 162

D 38 (Diss., Köln, Univ., 2018)

ISSN 1866-1807
ISBN 978-3-95806-298-6

Vollständig frei verfügbar über das Publikationsportal des Forschungszentrums Jülich (JuSER)
unter www.fz-juelich.de/zb/openaccess.



This is an Open Access publication distributed under the terms of the [Creative Commons Attribution License 4.0](https://creativecommons.org/licenses/by/4.0/),
which permits unrestricted use, distribution, and reproduction in any medium, provided the original work is properly cited.

Contents

Zusammenfassung	4
Abstract	6
I. Introduction	8
II. Theoretical background and state of the art	11
II.1 MLD-state of the art.....	11
II.2 Self-assembled molecular monolayers	13
II.3 Molecular deposition techniques	15
II.4 MLD deposition	15
II.5 Molecular bonding interaction	16
II.6 Arrangement of molecules in a SAM	18
III. Experimental techniques and sample preparation.....	20
III.1 Choice of substrates and substrate preparation	20
III.1.1 Cleaning procedure	20
III.2 MLD	21
III.2.1 Silanization mechanism	21
III.2.2 MLD setup, automatization and deposition process	22
III.3 In-situ characterization methods	24
III.3.1 Capacitive sensor	24
III.3.2 Sensor preparation	26
III.4 Ex situ characterization methods.....	29
III.4.1 Electronic measurement of molecules in the liquid state	29
III.4.2 Ellipsometry	30
III.4.3 Contact angle measurements	33
III.4.4 Surface potential measurement	34
III.4.5 AFM.....	37
III.4.6 Fluorescence microscopy.....	39
III.5 Cell culturing	41
III.5.1 PLL preparation	41
III.5.2 Neuronal culture	41
III.5.3 HL-1 cell culture	42
III.5.4 Live-dead imaging	42
IV. Results and discussion	43

IV.1 In situ analysis of the growth and dielectric properties of organic SAMs	43
IV.1.1 In situ controlled SAM deposition	44
IV.1.2 Dielectric properties of SAMs	48
IV.2 Controlled engineering of oxide surfaces for bioelectronics applications using organic mixed monolayers	49
IV.2.1 Deposition of mixed molecular monolayers.....	50
IV.3 Engineering of cortical neurons growth density and enhancing MEA coupling via mixed SAMs ...	57
IV.2.1 PLL deposition on the mixed molecular SAMs	58
IV.2.2 Neuron growth density on mixed molecular SAMs.....	59
IV.2.3 Cell-chip communication	63
Summary	67
References	69
Erklärung	74
Lebenslauf.....	75

Zusammenfassung

Das Verständnis der Grenzschichten zwischen Zellen und implantierbaren Oberflächen ist einer der Schlüssel für die elektronische Ankopplung von anregbaren Zellen und bioelektronischen Bauelementen. Unterschiedliche Vorgehensweisen zur Modifizierung von Oberflächeneigenschaften mit dem Ziel der Verbesserung der Zelladhäsion oder Biokompatibilität sind in der jüngeren Vergangenheit eingeführt worden. Diese Verfahren haben z.B. zum Ziel, das Zellwachstum zu kontrollieren oder zu stimulieren und die elektronischen Signale der Zellen aufzunehmen. Trotz all dieser Ansätze ist immer noch nicht wirklich geklärt, wie man eine ideale Oberfläche in kontrollierter Weise für die mechanische und auch elektronische Kopplung optimieren kann.

In dieser Arbeit präsentieren wir daher eine neuartige Methode, die es erlaubt, die Abscheidung von molekularen Schichten in einer von uns konstruierten und aufgebauten MLD-Anlage (Molecular layer deposition) zum einen in-situ zu kontrollieren und zum anderen alle Prozessschritte beginnend mit der Aktivierung der Oberflächen, der eigentlichen Deposition der Moleküle und der anschließenden Desorption der überflüssigen Moleküle ohne Unterbrechung des Vakuums durchzuführen. Die so generierten selbstanordnenden Monolagen (SAM) können nicht nur online überwacht werden, die in-situ Vermessung der elektronischen Eigenschaften der Lagen zeigt auch das Potential dieser SAMs z.B. als sog. hochpermittives Material für die organische Elektronik (z.B. zeigen SAMs aus APTES eine Permittivität von 51).

Als zweites wird gezeigt, dass mit dieser Methode die Oberflächen und deren Eigenschaften gezielt modifiziert werden können. Dies wird am Beispiel von Silikonoxid und Polyimid gezeigt, das mit SAM aus APTES und GLYMO mit unterschiedlichem Mischungsverhältnis beschichtet wird. Die Eigenschaften der resultierenden molekularen Monolagen (z.B. effektive Dicke, Hydrophobizität oder Oberflächenpotential) zeigen eine perfekt lineare Abhängigkeit von der Zusammensetzung der Schicht.

Mit Hilfe des Mischungsverhältnisses der molekularen SAMs kann des weitern auch die Dichte von zusätzlichem Polylysine, das üblicherweise als Zwischenschicht für Zelleexperimente und Wachstum verwandt werden kann, kontrolliert werden. Dies weist darauf hin, dass die Verwendung der gemischten molekularen Lagen auch eine ideale Möglichkeit darstellt, anorganische Oberflächen für bioelektronisch Anwendungen zu optimieren.

Schließlich konnten gezeigt werden, dass mit Hilfe der gemischten molekularen SAMs auch das Wachstum von neuronalen Zellen beeinflusst und die elektronische Zell-Chip-Kommunikation verbessert werden kann. Wir konnten demonstrieren, dass die Verwendung der molekularen Schichten die Zellkopplung stark verbessern konnte, elektronische Signale von bis zu 10mV konnten für das Aktionspotential von HL-1 Zellen mittels Multielektrodenarrays gemessen

werden. Die so mit SAMs präparierten Arrays könnten zu dem wiederverwandt werden, was die Produktivität steigen und die Kosten für Zellexperimente verringern kann.

Die neue MLD-Technologie mit der in-situ Depositionskontrolle könnte ein sehr gutes Instrument darstellen, das den Weg zu verbesserter oder sogar neuen bioelektronischen Anwendungen von der Bio- oder Molekülsensorik, bioelektronischen Plattformen bis hin zu elektronischen Zwischenschichten zwischen biologischen Objekten und Elektronik verbessern helfen kann.

Abstract

An in-depth understanding of the interface between cells and implantable surfaces is one of the keys for coupling electrically excitable cells and bioelectronics devices. Recently, different approaches for the tailoring of surface properties to enhance the cell adhesion or create biocompatible surfaces have been introduced. These approaches aim for instance to control the cell growth or stimulate and record electrical signals emanating from the cell. Nevertheless, it still remains an open question how to create an ideal surface in a precisely controllable way for cells to couple mechanically or/and electronically to various materials or electronics.

Here, we first present a novel in situ and extremely sensitive detection method for the analysis of the electronic properties of molecular layer during the molecular layer deposition using an in-house engineered and automatized molecular layer deposition (MLD) setup that allows to perform all process steps including surface activation, deposition of different molecules from the gas phase, and the desorption of superfluous molecules, resulting in the formation of a molecular self-assembled monolayer (SAM) without braking the vacuum. The method not only allows monitoring and optimizing the deposition of organic layers but also demonstrates the high potential of organic SAMs for instance in form of organic high-k layers in electronic devices (e.g. $\epsilon_{\text{SAM}} \approx 51$ in case of APTES).

Second, using this method, we modified the surface and surface properties of silicon oxide and polyimide by growing self-assembled monolayers comprising various compositions of two different molecules – APTES and GLYMO. The properties of the resulting mixed molecular monolayers (e.g. effective thickness, hydrophobicity, and surface potential) exhibit a perfect linear dependence on the composition of the molecular layer demonstrating that the surface properties can be tuned with these molecular layers.

Third, coating the mixed molecular layers with poly(L-lysine) (PLL) shows that the density of polymer which is commonly used as buffer layer for cell adhesion and growth, can be controlled by the composition of the organic layer as well. This indicates that the method might be an ideal way to optimize inorganic surfaces for bioelectronics applications.

Finally, we used the mixed molecular self-assembled monolayers to control the growth of neuronal cells and enhance the cell-chip communication. We demonstrate a strongly improved cell coupling and obtained high signals (up to 10 mV) for the action potential of HL-1 cells on multi electrode structures (MEA) covered with the mixed molecular layers. Additionally to this promising results in biocompatibility, the SAM covered MEAs could be reused for further cells experiments which would lead to increased productivity and reduced costs of the cell experiments.

In conclusion the novel MLD technology with in situ deposition control seems to be a very powerful tool and might pave the way to improved or even novel bioelectronics applications

ranging from bio- and molecular sensors to bioelectronics platforms that allows electronic interfaces with biological objects.

I. Introduction

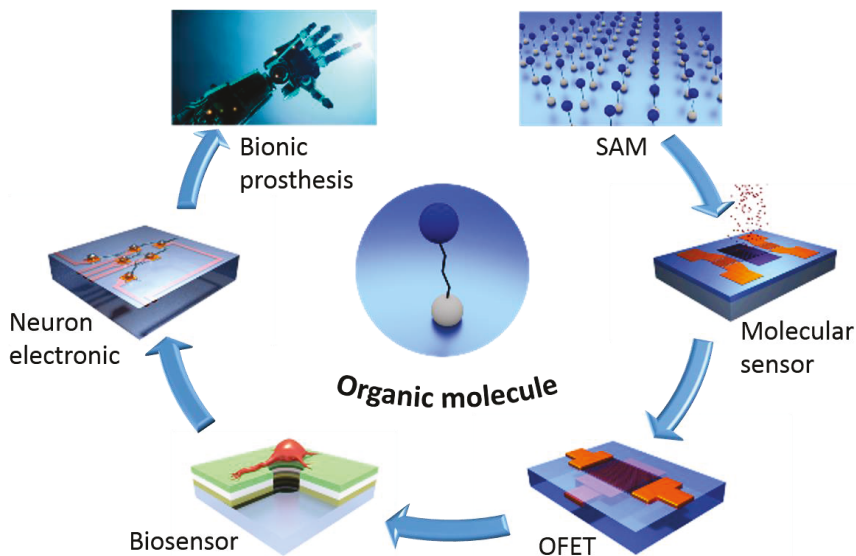


Figure 1. Development of organic electronics. From simple layers to complex bionic devices.

Atoms and molecules represent the building blocks of nature. Universe started with the formation of subatomic particles into simple atoms, the building blocks of inorganic materials. Only later molecules were developed and let first to simple organics and finally life itself.

Scientific and technological development might take a similar way. Taking for example electrical technology, it started with “simple” wires and bulky devices made to illuminate streets and houses with the light or to broadcast the radio signals. Improving and miniaturizing with the time, electronics came to the thin film nanotechnology for supercomputers. However, nowadays scientists are increasingly discussing the possibility of moving from inorganic to organic molecules as a replacement of existing or for novel devices.

Indeed, molecular electronics has several advantages over standard silicon based electronics:

- it offers higher complexity and packing density,
- it promotes further miniaturization of devices due to nano and subnano sizes of the molecules,

- there is almost unlimited resources of molecular supplies around us, which can be used for this approach,
- there is a wide range of applications from simple to extremely complex once.

As for the applications themselves, organic molecules in particular and bioelectronics in general can be used in different approaches:

- all biological systems communicate in a language of ions and molecules, whereas, modern technology relies on a language of electrons,
- devices based on molecular electronics possess a combination of both electronic and ionic/molecular conductivity,
- the chemical universality of molecular systems allows the inclusion of several functionalities in a single material - e.g. electrical and chemical functionality, and
- one might use self-assembly of molecules (similar to the epitaxy of atomic structures) to engineer a layer or an interface between inorganic and organic material for electronics or medical biocompatible system.

In spite of all its advantages, listed above, the relation of a molecular electronic turns out to be quite difficult. One of the main issues is to produce perfect organic layers, which could serve as electronic component, or act as a bioelectronics interface. Up to now most coating techniques rely on a deposition of molecules from the liquid phase. In most of these technologies precision and quality of a deposition are lacking. Therefore the search for a “perfect” and reproducible deposition technology for complex molecular monolayers is one of the big issues in this field. This is the aim of this work, we tried to develop and demonstrate a deposition technique for complex molecular monolayers tailored for bioelectronics applications.

This was done in the following steps:

First, we constructed and build an automatized MLD setup that allows to perform all deposition steps including surface activation, deposition of different molecules from the gas phase, and the desorption of additional molecules, resulting in the formation of a molecular self-assembled monolayer (SAM) without braking the vacuum.

Second, we developed a novel in situ and extremely sensitive detection method for the control of the deposition process the analysis of the electronic properties of the growing molecular layer.

Third, we demonstrated the modification of the surface and surface properties (e.g. effective thickness, hydrophobicity, and surface potential) of silicon oxide and polyimide by growing self-assembled monolayers comprising various compositions of two different

molecules – (3-aminopropyl)-triethoxysilane (APTES) and (3-glycidyoxypropyl)-trimethoxysilane (GLYMO).

Forth, we demonstrated the biocompatibility of the mixed molecular layers with and without poly(L-lysine) (PLL), and use the compositions of the mixed molecular monolayers to control the protein density, also the density and live/dead ratio of subsequently grown neuronal cells.

Finally, we demonstrated a strongly improved cell-chip coupling for HL-1 cells on multi electrode structures (MEA) covered with the molecular layers.

We consider that the technology developed in this work could represent an ideal tool optimization of inorganic surfaces for bioelectronics applications.

II. Theoretical background and state of the art

Due to of their various functionalities, which are achieved via different functional groups, self-assembled monolayers (SAMs) are often used for the modification of the surface of the substrates or represent essential components in simple and complex organic electronic devices. SAMs are also the essence of this work. In this chapter we present the background and state of the art of SAM preparation and properties including SAM structure, various types of SAMs and molecules, which are used in this work:

- (i) chapter II.1 summarizes the MLD-state of the art,
- (ii) chapter II.2 describes basics of self-assembled molecular monolayers,
- (iii) chapter II.3 shows various techniques of surface modification for tailoring their properties,
- (iv) in chapter II.4 we introduce the molecular layer deposition (MLD) method from the gas phase, which provides exquisite control over film thickness, composition, and conformality at the molecular level.
- (v) then, in chapter II.5, we describe possible molecular bonding interaction of SAMs on the surface
- (vi) and finally, in chapter II.6 we calculate density of SAMs used in this onto Si/SiO₂ surface for different molecular arrangements.

II.1 MLD-state of the art

Many high-end technologies rely on our capability to fabricate thin films and coatings with on-demand tailored compositions and architectures in a highly controlled way. The atomic layer deposition (ALD) technique is capable of producing high-quality nanometer-scale thin films in an atomic layer-by-layer manner using molecules as a carrier for the atoms to be deposited. Molecular layer deposition (MLD) works similar, however in MLD the molecules themselves form the layer, i.e. a molecular layer.

The history of ALD goes back to the 1970s¹⁻⁴. Traditionally, ALD has been used to fabricate rather simple well-known inorganic materials, such as binary oxides and nitrides. The range of

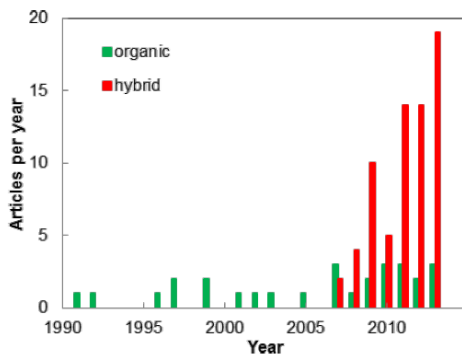


Figure 2. Number of articles annually published featuring organic and hybrid inorganic-organic thin films deposited by MLD and ALD/MLD

materials was fundamentally broadened by experiments producing organic polymers in the 1990s by a variant of ALD, now commonly known as molecular layer deposition (MLD), named after the molecular layer-by-layer fashion the film grows during the deposition⁵⁻⁹. Then – most excitingly – in the late 2000s the two techniques, ALD and MLD, were combined to produce inorganic–organic hybrid materials (Figure 1), making it possible to synthesize totally new material families with versatile characteristics, which are not accessible by any other existing technique¹⁰⁻¹⁴. In the combined ALD/MLD process organic molecules are covalently bonded to the metal atoms and vice versa, forming periodic thin-film structures that can be imagined to consist of either interlinked hybrid inorganic–organic polymer chains of essentially identical lengths or alternating two-dimensional (2D) planes of inorganic and organic monolayers. The hybrid thin films may not only possess properties combined from those of the two parent materials, but may also have completely new material properties, making them excellent candidates for a wide range of applications. Possible uses for the hybrid ALD/MLD films include optoelectronic devices, sensors, flexible electronics, solar cell applications, and protective coatings, to name only a few. It is also straightforward to make porous structures from the ALD/MLD grown hybrids by removing the organic part by simple annealing or wet-etching procedures^{15,16}. Further tuning of material properties may be achieved by combining different inorganic, organic and hybrid layers into various thin-film mixtures, superstructures and nanolaminates. For example, precise control of the refractive index is extremely important in optical applications¹⁷, while control of the electrical properties is required for storage capacitors, non-volatile memories as well as for transparent thin-film transistors^{18,19}. Moreover, the tunability of the surface roughness is advantageous when fabricating gas sensors²⁰. Over the years a number of excellent reviews featuring various types of ALD processes have been published, most recently, e.g., by Puurunen⁴, George²¹, Miikkulainen et al.²², and Knez et al.²³.

In details: George et al.²¹ discusses the surface chemistry of MLD grown materials, addressing the problems which arise when using organic precursors in the growth process; Leskelä et al.²⁴ shortly reviews the novel materials fabricated by ALD and MLD; George²⁵, George et al.²⁶ and Lee et al.²⁷ focus on metal alkoxide thin films; Yoshimura et al.²⁸ discusses a possibility to utilize MLD in cancer therapy applications; King et al.²⁹ describe fine particle functionalization by ALD and MLD; and the review by Zhou et al.³⁰ covers all the organic interfaces fabricated by MLD³¹; Gilles et al.³² investigates chemical modification of silicon surfaces via MLD for applications in soft lithography and Greben et al.³³ performs modification and characterization of potential bioelectronics interfaces via MLD. Nevertheless, although the introduction of the MLD method dates back two decades, the number of articles featuring purely organic thin films is still quite limited.

II.2 Self-assembled molecular monolayers

Structurally well-defined organic monolayers on solid surfaces allow experimentalists to simplify and model a large variety of interfacial phenomena that are often impossible or difficult to establish at "natural" interfaces. Organosilane reagents have attracted significant attention in recent years due to the production of functionalized thin films on silicon oxide and other oxide substrates that can be used for a variety of technological applications. For example aminosilanes may serve as the foundation layer for the fabrication of various biosensor and bioarrays,³⁴⁻³⁸ they can be used for the production of arrays of metal nanoparticles³⁹⁻⁴¹, energy storage devices⁴², probe protein and cell adhesion⁴³⁻⁴⁵, and, furthermore, it is known to be compatible to graphene⁴⁶.

SAMs are ordered molecular assemblies that are formed spontaneously by the adsorption of a surfactant with the specific affinity of its head group to the surface (Figure 3).

The SAMs consist of:

- (i) an end or functional group, which can possess different functionalities, e.g. it could be different by charge,
- (ii) the backbone, which can be a chain of isomers (typically alkyl chain), with a given length, and
- (iii) a head group, which is chemisorbed to a specific substrate.

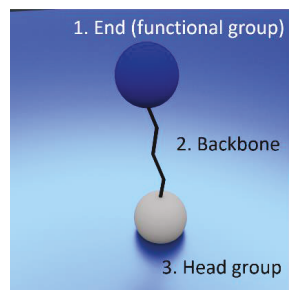


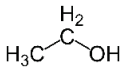
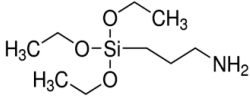
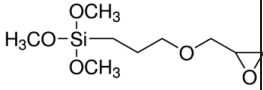
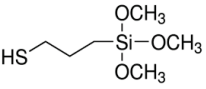
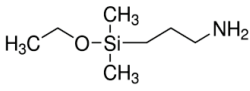
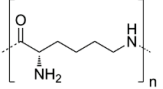
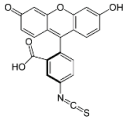
Figure 3. Schematic structure of self-assembled molecule.

The head group reacts with specific sites on the surface creating an attachment through a chemical bond. Generally the energies associated with the chemisorption are of the order of hundred kJ/mol. Because of the exothermic interaction between substrate and head group, molecules tend to occupy every available binding site on the surface. The deposition represents a dynamic process consisting of molecules being physically adsorbed and then chemically adsorbed or desorbed. This way they shall form the SAM. The functional group determines the properties of the SAM surface, e.g. wettability and reactivity.

The most well-known and extensively studied SAMs on silicon based substrates are organosilanes. Organosilanes can be used as a SAM system for hydroxylated substrates or substrates with a thin water layer. A possible substrate for the formation of silane SAMs is oxidized silicon, which will be further discussed in section III.2.3. Nevertheless, a variety of different substrates can be coated with silane SAMs such as Si-wafers, mica, PDMS, glass or even metals (e.g. Al with a top oxide layer). SAMs prepared on smooth surfaces like Si wafers exhibit extraordinary properties in terms of chemical homogeneity, ultra-low surface roughness and controlled wettability. The latter can be varied from hydrophilic to hydrophobic, depending on the end group of the silane. Silane layers in particular are mechanically robust, thermally stable up to at least 100°C and are not subject to swelling in the presence of solvents. These properties render silane-coated substrates ideal model surfaces to study a wide range of physical, chemical and biological phenomena such as adhesion,

adsorption or coupling of bio objects. They act, for example, as a buffer layer between silicon based surfaces and bio objects such as proteins and cells⁴³⁻⁴⁵. Table 1 summarizes the different molecules and their properties that are used in this work.

Table 1. Molecules and their properties used in this work including structure, experimentally determined permittivity ϵ_{liquid} in the liquid state, and experimentally determined thickness h_{mol} of the SAM. Additionally literature values for the length l_{mol} (long axis) of the molecules are given.

Molecules/liquids (abbreviation) and molecular formula	Structure	ϵ_{liquid} (T=300 K, 1 kHz)	h_{mol} [nm]	l_{mol} [nm]
Ethanol C ₂ H ₆ O		24.3	---	---
(3-Aminopropyl)-triethoxysilane (APTES) C ₉ H ₂₃ NO ₃ Si		6	0.75±0.05	0.8±0.1 ⁴⁷
(3-Glycidyloxypropyl)-trimethoxysilane (GLYMO) C ₉ H ₂₀ O ₅ Si		8.8	0.2±0.05	---
(3-Mercaptopropyl)-trimethoxysilane (MPTES) C ₆ H ₁₆ O ₃ SSi		5.5	0.55±0.05	0.5±0.1 ⁴⁸
3-(Ethoxydimethylsilyl)-propylamine (APDMES) C ₈ H ₂₂ NOSi		6	0.45±0.05	0.65±0.01 ⁴⁹ , 0.36±0.01 ⁵⁰
Poly (L-lysine) (PLL) (C ₆ H ₁₂ N ₂ O) _n		---	---	---
Fluorescein isothiocyanate (FITC) C ₂₁ H ₁₁ NO ₅ S		---	---	---

II.3 Molecular deposition techniques



Figure 4. Various techniques for the deposition of molecules: (a) solution casting, (b) stamp printing, and (c) inkjet printing.

There are different techniques to deposit molecules from the liquid state (see Figure 4) such as solution casting, stamp printing or inkjet printing. The most common technique is the immersion of a freshly prepared or clean substrate into a diluted molecular solution at room temperature (see Figure 4a). This widely used procedure originates from early studies of SAMs. Dense coverages of adsorbates are obtained quickly from millimolar solutions (milliseconds to minutes), but a slow reorganization process requires times of the order of hours to maximize the density of molecules and minimize the defects in the SAM. There are, however, a number of experimental factors that can affect the structure of the resulting SAM and the rate of formation which are for instance the choice of solvent, temperature, concentration and purity of the adsorbate, immersion time, concentration of oxygen in the solution, cleanliness of the substrate, and chain length or, more generally, structure of the adsorbate⁵¹.

However, SAM coatings that are grown from the liquid phase have significant drawbacks, such as complicated process control, the generation of large amounts of contaminated effluents, insufficient stiction prevention, and high production costs. Vapor-phase processes can eliminate some of the problems that are seen in liquid-based processes and thereby attract strong attention. In vapor-phase processes, the precursor chemistry is easily controlled, efficient mass transport ensures coating of high-aspect-ratio structures, and self-limiting surface reactions lead to conformal monolayer coverage. It has been shown that the performance of SAM coatings that are grown in vapor phase is comparable or superior to SAMs that are grown in liquid phase. Moreover, vapor-phase processes have better reproducibility and might be adapted easily to industrial requirements.⁵²

II.4 MLD deposition

A related dry process known as molecular layer deposition (MLD) can provide exquisite control over film thickness, composition, and conformality at the molecular level. MLD utilizes sequential, self-limiting surface reactions to build up a thin film on a substrate, in the optimized case one molecular layer at a time. Figure 5 illustrates a generic MLD scheme using sequential and self-limiting surface reactions. A MLD cycle can include several molecule doses with a

purging step immediately following each dose to remove excess molecules from the reaction system. During each dose step, the given molecules react with surface reactive groups via the corresponding linking chemistry, such as amide coupling or urea coupling, add a molecular layer on the surface, and leave the surface terminated with new reactive sites for further film growth. The self-limiting nature of the surface reactions results in several characteristic features of MLD film growth, such as a linear growth rate and saturation behavior with respect to the molecule doses.

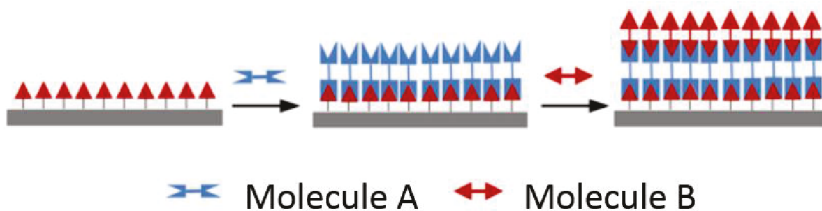


Figure 5. Schematic of a MLD process based on self-limiting surface reactions for the preparation of molecular multilayers.

MLD has many advantages over the solution film deposition methods. First, its self-limiting nature ensures excellent coating conformality, even for high-aspect-ratio features. Second, its layer-by-layer growth behavior enables fine tuning of the molecular composition. Hence, MLD can serve as a powerful deposition technique for thin molecular films of many kinds and thereby address the challenges that nanotechnology brings to organic layer coating.³⁰

II.5 Molecular bonding interaction

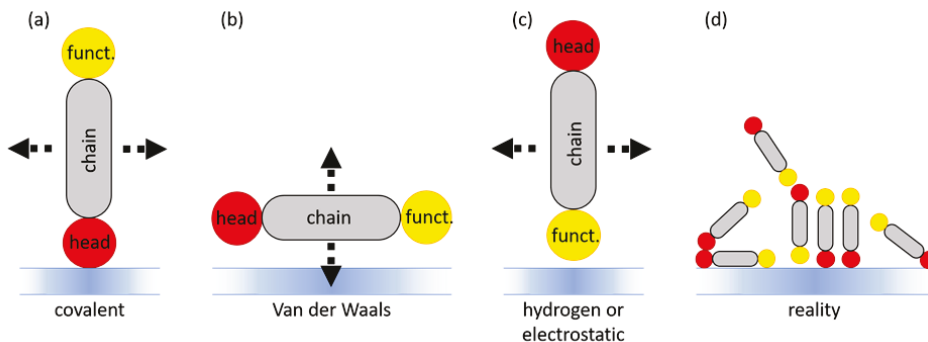


Figure 6. Binding options of self-assembled molecules; head, chain, and funct. symbolizes the head group, chain, and functional group of the molecule.

Actually, Figure 5 shows an ideal case of the bonding of a molecule at the substrate. In reality, molecules can connect to a surface in different ways (see Figure 6). The possible bonding interactions that are relevant in this work are:

(i) Van der Waals force. The van der Waals force is the weakest of the atomic bonding interactions (0.4-4.0 kJ/mol). It typically occurs in between atoms or molecules whose valence shell is fully occupied by electrons (e.g. noble gases). Due to fluctuations in their electron shells repeated dipole moments are created and destroyed in the molecule. These fluctuations introduce a dipole moment in neighboring surfaces, which leads to the bonding of the molecules at the surface.

(ii) Ionic bonds. The ionic bond is based on the electrostatic interaction between oppositely charged ions. In case of molecular deposition the head group of the molecule and the substrate surface should be of opposite charge. The interaction is typically of the order of approximately 20 kJ/mol.

(iii) Covalent bonds. A covalently bond or molecular bond is a chemical bond that involves the sharing of the electrons between atoms. Due to shared electrons an attractive force that is typically >60 kJ/mol is created. Covalently bonded molecules are not conductive, because conductance needs free or dislocated electrons. Only exceptions are conjugated covalent bonds (e.g. graphene).⁵³

(iv) Hydrogen or electrostatic bonds. A hydrogen bond represents a combination of a covalent and an ionic bond. If a covalent bond between hydrogen and an atom with high electronegativity (e.g. oxygen or nitrogen) is formed, hydrogen donates its electrons almost completely to the partner. As a result hydrogen is positively charged and can bind to an electronegative atom (ionic binding). Due to the size of the positively charged hydrogen (proton), only two atoms can be connected via one hydrogen bond.⁵³ The strength of the hydrogen bond is approximately 12-30 kJ/mol.

II.6 Arrangement of molecules in a SAM

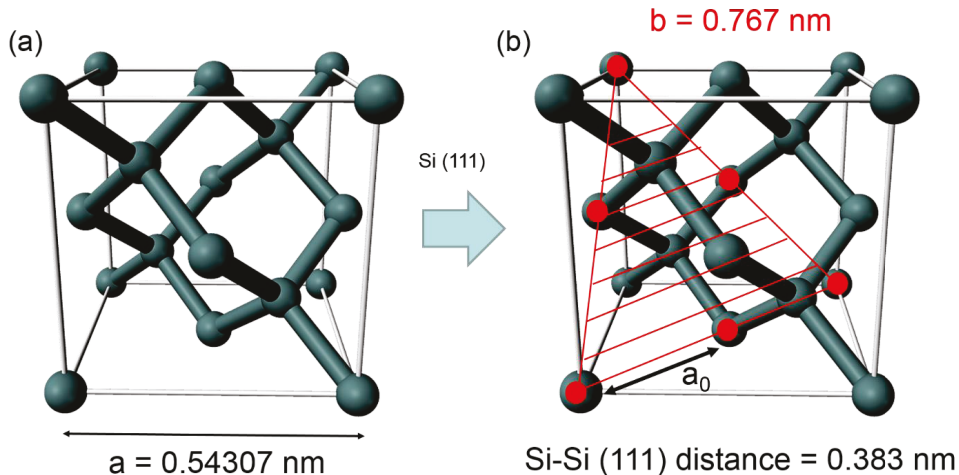


Figure 7. Silicon crystallizes in a diamond cubic crystal structure (a) and (111) silicon plane (b) showing the distribution of Si atoms on the (111) Si surface.

In addition to the possible bonding interactions of molecules with the substrate surface it is important to discuss possible molecule distributions on the surface. This provides among others an idea on the expected density of molecules which for instance affects the capacitive signal (see chap. III.3.1).

If we assume covalent interaction between molecules and surface the possible molecule density depends on the areal density of Si atoms in case of (111) Si, which is used in this work (see Figure 7). Silicon, crystallizes in a diamond cubic crystal structure with a lattice spacing of $a = 0.54307 \text{ nm}$. The distance between adjacent Si atoms in the (111) Si plane is:

$$a_0 = \frac{a\sqrt{2}}{2} = 0.383 \text{ nm}. \quad (1)$$

In order to estimate the density of SAMs on the surface of Si (111) we will consider two extreme cases:

- (i) the “ideal case” when all molecules are covalently bonded with their head group (see Figure 7a) and
- (ii) the “worst case” when all molecules are additionally electrostatically bonded (see Figure 7b).

Considering the molecule APTES with a chain $c \approx 0.5 \text{ nm}$, a length of each bond $b \approx 0.1 \text{ nm}$, a diameter of the Si atom $d_{\text{Si}} \approx 0.21 \text{ nm}$, and size of the amino group $d_{\text{NH}_2} \approx 0.3 \text{ nm}$, we can calculate the expected distance l between adjacent molecules if distortions are neglected for both cases:

$$\text{ideal case: } l_{fa} = 2bc\cos 45^\circ + d_{\text{Si}} = 0.354 \text{ nm} \quad (2)$$

$$\text{worst case: } l_{na} = b + d_{\text{Si}} + c + d_{\text{NH}_2} = 1.11 \text{ nm} \quad (3)$$

where l_{fa} the distance between molecules in fully assembled ideal state (see Figure 8a) and l_{na} is the distance between molecules in not assembled worst state (see Figure 8b).

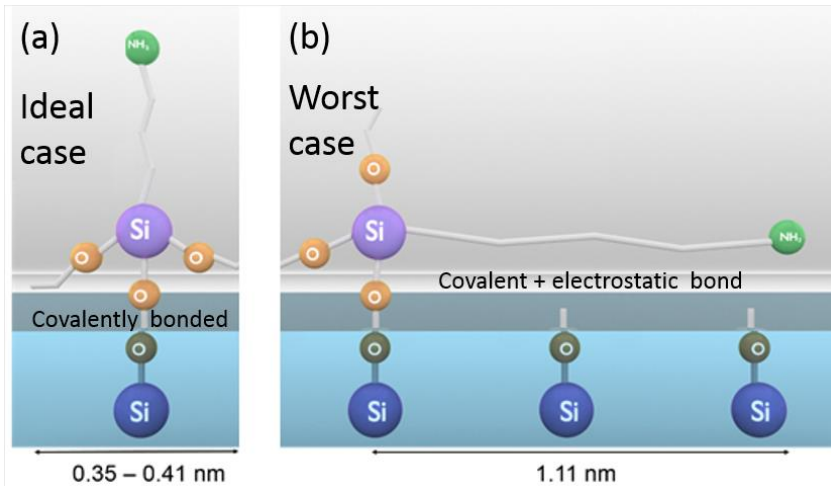


Figure 8. (a) Fully assembled APTES molecule and (b) not assembled APTES molecule on the surface of Si/SiO₂.

Using these rough estimations, we can estimate how molecules might be distributed on the surface in both extreme cases. In the ideal case the distance between APTES molecules ($l_{fa} \approx 0.354 \text{ nm}$) and the spacing of Si on the Si (111) surface ($a_0 \approx 0.383 \text{ nm}$) match perfectly. Considering, that there are no defects in the Si structure we can expect an APTES density of 9 mol/nm^2 in the “ideal” case (Figure 8a). In the worst case, one APTES molecule “occupies” three Si atoms. Therefore we would expect a three times smaller density of APTES in this case, i.e. 3 mol/nm^2 in the “worst” case (Figure 8b). This implies, that some properties can also vary strongly depending on the quality of the SAM. In chapter III.4.1 we will demonstrate that for instance the permittivity of the SAM can be extremely large for high quality SAMs.

III. Experimental techniques and sample preparation

For our research we need a series of experimental techniques ranging from the deposition and characterization of the molecular layers to the preparation and analysis of cells on the molecular layers. The resulting techniques are listed and sketched in this chapter

- (i) starting with the choice and preparation of the substrates, which includes the cleaning routines (see chap. III.1),
- (ii) the deposition device and deposition process of self-assembled molecular monolayers (SAMs), including the principles of the SAM formation (see chap. III.2), followed by
- (iii) the in situ characterization methods, which were used to monitor and control the deposition of the molecular monolayers (see chap. III.3.), and finally
- (iv) the ex situ methods such as ellipsometry, contact angle measurements, and streaming potential measurements to determine the quality of obtained films (see chap. III.4).

III.1 Choice of substrates and substrate preparation

In this study, we used borosilicate glass (Präzisions Glas & Optik GmbH) as the substrate for the in situ capacitive sensor and p-doped silicon (Si (111)) (Si-Mat, 3.6-6.5 $\Omega \cdot \text{cm}$) with a 90-nm-thick SiO_2 termination layer for the ex situ ellipsometry, contact angle, and AFM measurements, respectively. Both types of substrates are equally suited for biological applications and compatible with most electronic circuits. Furthermore, molecules with silane head groups, such as (3-aminopropyl)-triethoxysilane (APTES), can be chemisorbed to these substrates forming covalent bonds.

III.1.1 Cleaning procedure

Since the formation of the SAMs on the substrate depends strongly on the surface quality⁵⁴, cleaning the sample surface is very important.

- First, the substrates are cleaned in acetone ($\geq 99.9\%$, Sigma-Aldrich) for 5 minutes in an ultrasonic bath (25 °C at 320 W power and 37 kHz frequency).
- Then they are cleaned in isopropyl alcohol (2-propanol, $\geq 99.5\%$, Sigma-Aldrich) also in an ultrasonic bath (5 min at 25 °C, 320 W and 37 kHz).
- Finally, the substrates are dried with nitrogen.

For the ex situ thickness measurement of the SAMs, we performed reference measurements on the SiO_2 -terminated Si samples via ellipsometry (SE 800 PV) directly after the cleaning procedure.

An 81-point mapping via ellipsometry was performed for each sample in order to determine the homogeneity of molecular distribution on the surface after silanization (see also chap. III.4.2).

III.2 MLD

In the following we describe

- (i) the silanization mechanism i.e. the way molecules react with the substrate surface and form a molecular layer (see chap. III.2.1),
- (ii) then we present the new and self-made molecular layer deposition (MLD) setup and the deposition process (see chap. III.2.2).

III.2.1 Silanization mechanism

As we already discussed in section II.1, the head group of the molecule always has to be considered together with the surface to which this molecule is about to bind. Consequently, silanes are the molecules that form a silanol bond (Si-O-Si) at the surface. Typically, the head group of silanes is hydrated and easily undergoes a chemisorption on an activated surface that also possesses silanol bonds. Schematically, the silanization process is shown in Figure 9.

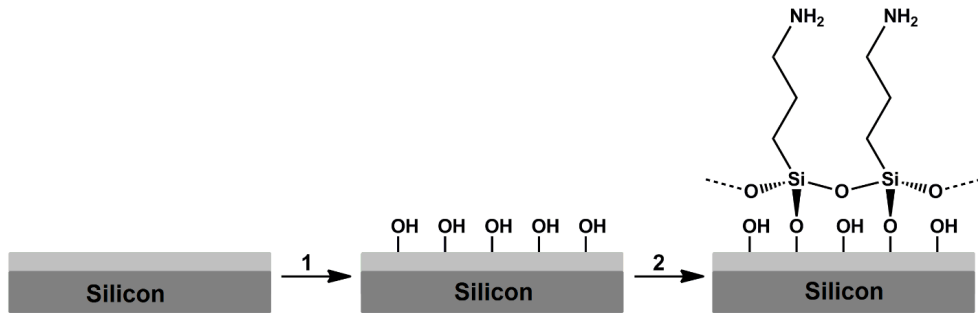


Figure 9. Schematic presentation of the silanisation: (1) ozone treatment, (2) APTES deposition.

From this figure, it is clear why the Si surface has to be activated, in order to allow a perfect coverage of the Si with molecules. The activation of the silicon surface represents a reconstruction of the silanol surface bonds. Freshly prepared SiO₂ exhibits silanol groups Si-OH on the surface. When exposed to a humid environment the silanol groups undergo a condensation reaction, forming more stable siloxane groups Si-O-Si which reduce the reaction with the molecules during deposition⁵⁵. In this state, the Si surface has less open bonds and the quality of the silane deposition

would be poor. An activation with an oxygen plasma recovers the silanol groups and leads to a homogenous, and dense coverage of the surface with molecules.

III.2.2 MLD setup, automatization and deposition process

Figure 10 shows a schematic sketch of the MLD setup that allows the surface activation and subsequent deposition of different molecules from the gas phase without braking the vacuum. It consist of

- (i) an ozone generator (a modified commercial microwave oven) for cleaning and activation of the surface,
- (ii) the sources (typically two) that contain the molecules and that are connected via a valve with the main recipient,
- (iii) the gas system consisting of (a) a controllable gas inset of oxygen (to the generator) and nitrogen (to the sources) and (b) a down-stream controlled pump system (a turbo pump and an oil-free prepump) that allows a stabilization of the pressure in the regime of 10^{-2} mbar to 50 mbar and a minimum pressure of about 10^{-5} mbar, and
- (iv) the main recipient, i.e. the MLD deposition chamber where we can place the different carriers for instance the sensor (left) for in-situ monitoring and analysis the deposition and a number of substrates (right) for the deposition of the molecular layers.

These substrates are subsequently used for ex-situ analysis like ellipsometry, wetting angle measurements, streaming potential experiments, and biological experiments like PLL coating of cell growth. The setup is atomized using a computer and a self-written LabVIEW program. The different process steps that take place during the deposition process are described in the following.

Surface activation. After the cleaning process and the ellipsometry, the Si substrate is placed in the deposition chamber next to the capacitive sensor for the *in-situ* control. The chamber is evacuated (10^{-5} mbar) and then filled with pure oxygen gas (99.9%) with a pressure of 1 mbar. A RF-discharge is generated which generates ozone in a separate chamber (see Figure 10). Due to the gas flow, the ozone is directed to the substrates and capacitive sensor in the deposition chamber. The ozone treatment is applied for 3 minutes, it leads to

- (i) a removal of organic molecules from the walls of the chamber and the surface of the sensor and the substrates, and
- (ii) an activation of the surface of the samples and the sensor.⁵⁵⁻⁵⁷

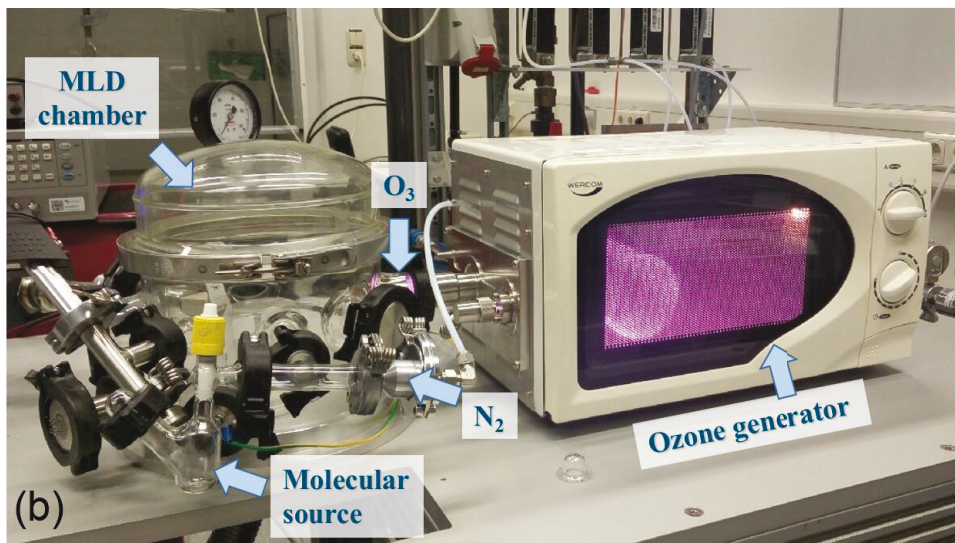
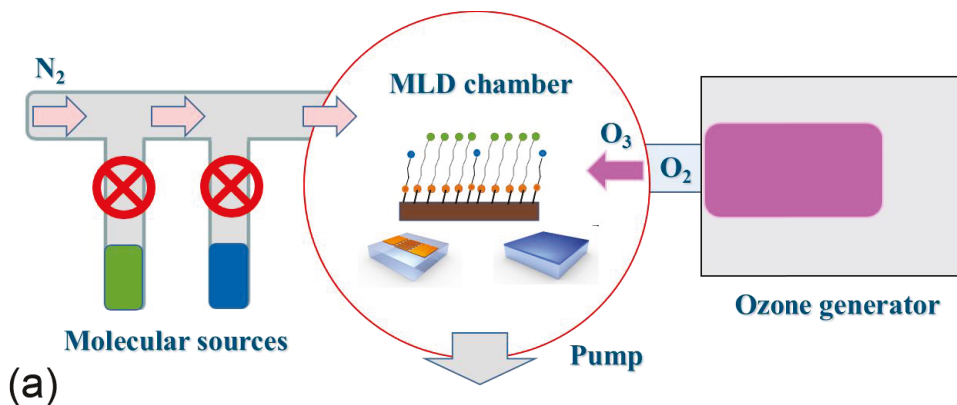


Figure 10. (a) Schematic of the MLD setup and (b) photo of the working setup including (from left to right) the molecular sources with valves for the different molecules (shown in green and blue), the main deposition chamber with a depiction of a deposited mixed molecular layer and two substrates for the ex situ analysis as well as the ozone generator used for cleaning and surface activation prior to each deposition process.

Deposition process. After the oxygen surface treatment, the oxygen is removed from the deposition chamber, and the process parameters (N_2 pressure and flow) are established and stabilized. Typically N_2 pressures of 0.1 mbar to 10 mbar are established. The actual pressure depends on the vapor pressure of the molecule that is evaporated. By manual opening of the valve of source, the deposition of the molecules starts. Closing the valve terminates the active deposition process. Nevertheless, as we will discuss later, the formation of the SAM is not necessarily accomplished at this point. Due to the separate molecular sources (typically two sources are used) it is possible to perform either sequential or simultaneous deposition of several types of molecules. In order to allow a precise control of the deposition and especially ratio of the different molecules, usually a sequential molecular deposition is chosen. In this work this has also the advantage, that we could choose different N_2 pressures for the different deposition steps.

Post treatment. After closing the valve (termination the active deposition process), the deposition of molecules is stopped (there might be a small amount of redeposition of molecules from the glass walls of the MLD chamber) and desorption of molecules from the surface dominates the growth process. As a consequence, the thickness of the molecular layer decreases steadily and, finally, the layer thickness approaches a single monolayer, i.e. one continuous layer of molecules on the surface of the sensor and the substrates. In order to accelerate the desorption process the MLD chamber is purged with N_2 . After the substrates are taken out from the MLD recipient for the post processing procedures (ex situ measurements), the deposition chamber is closed, evacuated and activated in order to remove all organic components from the walls and the sensor and avoid the possible contamination of subsequent substrates.

III.3 In-situ characterization methods

The most important ingredient of the deposition setup is the new sensor type that was specially developed for the characterization and the control of the molecular deposition. In this section we discuss

- (i) the working principle of this sensor (see chap. III.3.1) and
- (ii) the process of sensor preparation (see chap. III.3.2)

III.3.1 Capacitive sensor

A specially developed capacitive sensor was developed for the in situ electronic characterization and control of the deposition.⁵⁷ The sensor (see Figure 11) is based on planar interdigitated electrodes (IDE) (see Figure 11a and b) that allow the recording of dielectric permittivity, dielectric losses, and conductivity of the molecular layer throughout the entire deposition process.

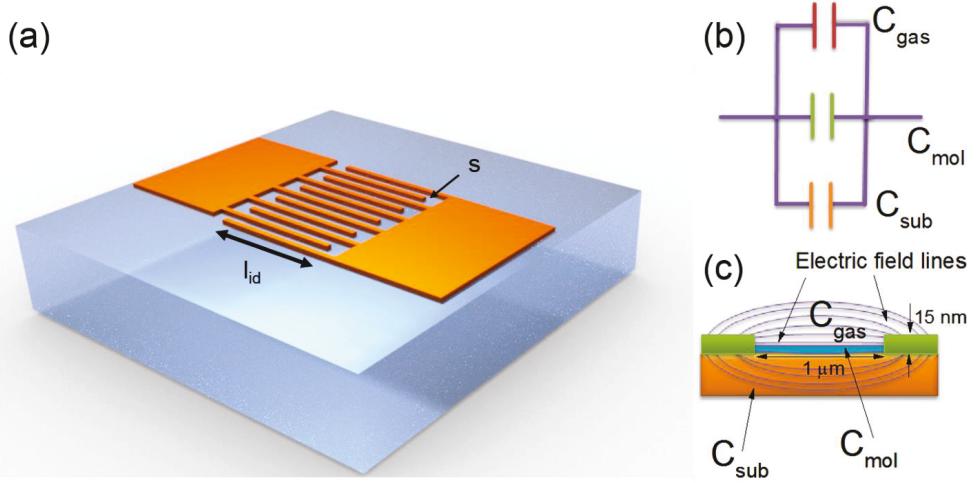


Figure 11. (a) Model of the interdigitated structure of the capacitive sensor, (b) electronic equivalent of the partial capacitance model, and (c) model of the field distribution of the capacitive structure with molecules between the electrodes.

The total capacitance C_{total} of the sensor is given by the sum of the different contributions:

$$C_{total} = C_{gas} + C_{sub} + C_{mol} = C_{ref} + C_{mol}, \quad (4a)$$

the losses are given by:

$$C_{total} * \tan\delta_{total} = C_{gas} * \tan\delta_{gas} + C_{sub} * \tan\delta_{sub} + C_{mol} * \tan\delta_{mol} = C_{ref} * \tan\delta_{ref} + C_{mol} * \tan\delta_{mol}, \quad (4b)$$

where C and $\tan\delta$ represent the capacitance and losses, respectively, and the subscripts represent the contributions of the gas (N_2 , O_2 , atmosphere or vacuum) above the sensor, the substrate, and the molecular layer, respectively. The reference $C_{ref} = C_{gas} + C_{sub}$ represents the capacitance before deposition, i.e. the capacitive signal without molecules. The change of the capacitance during deposition provides the resulting capacitive contribution of the molecular layer. The permittivity ϵ_{mol} of the molecular layer can be evaluated using the planar capacitance model:⁵⁸⁻⁶⁰

$$\epsilon_{mol} = \frac{C_{mol}}{\epsilon_0} \left[\frac{l}{\frac{4}{\pi} \ln 2 + \frac{s}{h_{mol}}} \right]^{-1}, \quad (5)$$

where ϵ_0 is the vacuum permittivity, s represents the gap between the electrodes, and h_{mol} represents the thickness of the molecular layer. The parameter l represents the effective length of the electrodes. In case of an interdigitate structure (see Figure 11a) l is given by

$$l = (2n - 1) * l_{id} \quad (6)$$

With n representing the number of fingers and l_{id} the overlapping length of the fingers (see Figure 11a).

Since the gap between the electrodes is usually significantly larger than the thickness h_{mol} of the molecular layer we can simplify the equation (5) to:

$$\epsilon_{mol} \approx C_{mol} \frac{s}{\epsilon_0 l h_{mol}}. \quad (7)$$

Similarly, the losses of the molecular layer can be evaluated.

III.3.2 Sensor preparation

Two different methods of lithography are used in the institute, the optical lithography and the e-beam lithography. Due to the optimizing process of the sensors in this work, we need a high flexibility, therefore the e-beam lithography is the better choice. Also, the resolution of the e-beam lithography is approximately $10 \text{ nm}^{\text{61}}$, which is helpful for creating perfect interdigitated electrodes. The optical lithography has typically a 10-100 times lower resolution depending of the method.

For the sensor system, a special design has been developed (using AutoCAD 2013), which actually consists of

- a resistive temperature sensor (4-probe), that uses separate pairs of current-carrying and voltage-sensing electrodes to make more accurate measurements than the simpler and more usual two-terminal sensing, and
- 3 different interdigitated electrode (IDE) structures, which can be used as capacitive or resistive sensors (see Figure 12a-b).

The IDEs of the capacitor consists of a combination of a Ti (5-nm-thick) and a Pt (10-nm-thick) layer and forms a capacitor with a gap of $s = 1 \mu\text{m}$ and an effective length of $l = 10.8 \text{ mm}$ (73 fingers with an overlapping gap length of $150 \mu\text{m}$). The large gap size of $1 \mu\text{m}$ was chosen in order to simplify the analysis and ensure a homogeneous deposition of molecules between the electrodes, whereas the large effective length of 10.8 mm led to a high sensitivity of the sensor. The sensors are prepared via e-beam lithography and the lift-off

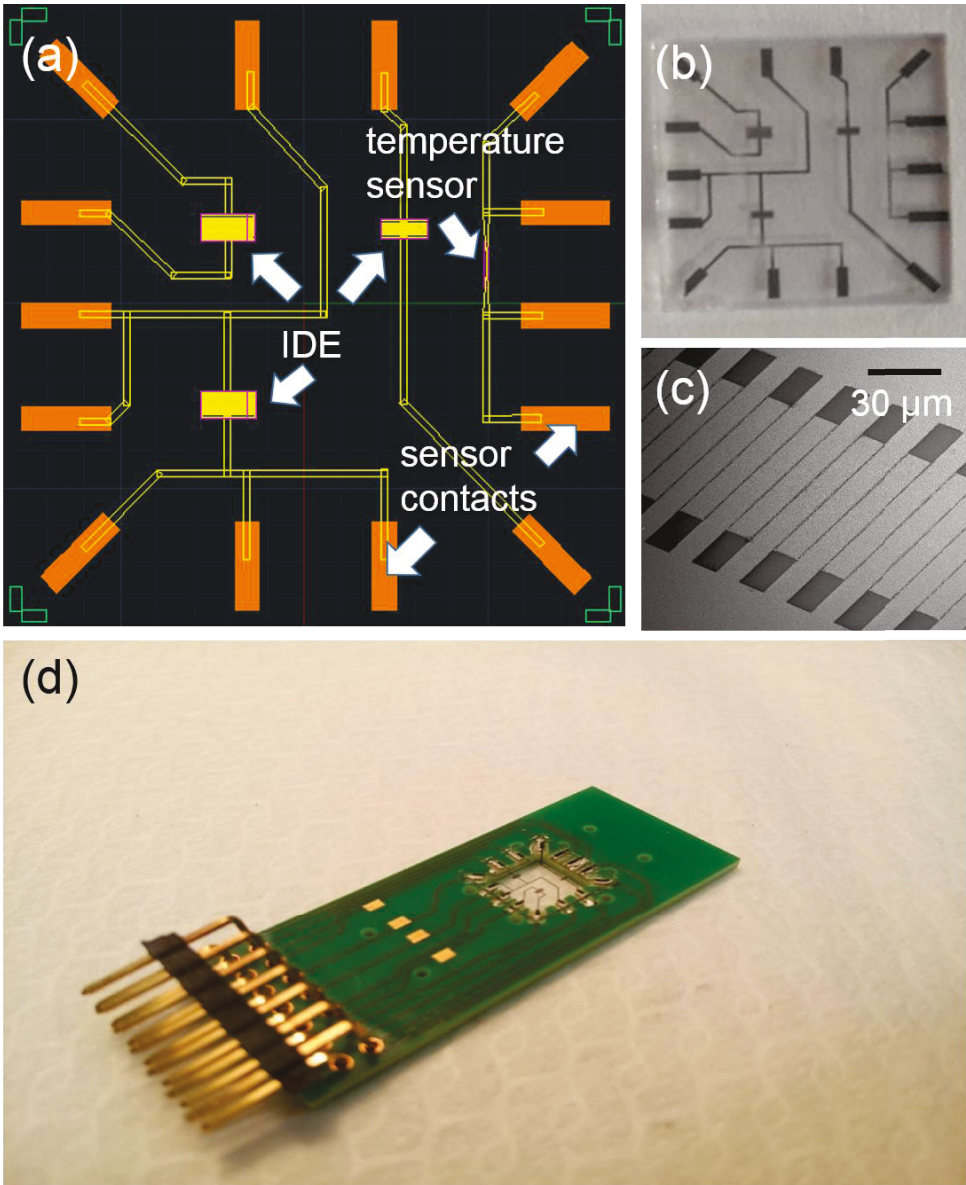


Figure 12. (a) A sensor design made in the AutoCAD for the e-beam writing, (b) the sensor with a size of $10 \times 10 \text{ mm}^2$. Figure (c) shows an SEM image of one interdigital structure of this sensor. The IDE has a finger length of $300 \text{ }\mu\text{m}$ and a distance of $2 \text{ }\mu\text{m}$. (d) Image of the complete sensor system including contacts, sample holder and a $10 \times 10 \text{ mm}^2$ borosilicate sample with IDTs.

technique on nonconductive borosilicate glass using a specific recipe. The different steps are sketched in and described in detail in the following:

Cleaning. In the first step the surface is cleaned. The glass substrates ① are immersed in acetone for 5 min in an ultrasonic bath at the highest power. In order to remove the acetone, the process is repeated with propanol.

Photoresist. The photoresist poly(methyl-methacrylate) (PMMA AR-P 669.07) is spin-coated on the substrate using 4000 rpm for 60 s. The substrate should be covered totally with resist and the thickness of the PMMA should be approximately 700 nm. After spin-coating the sample should be placed on a 120 °C hot plate as fast as possible and remain there for 30 min. On the way from the spin-coater to the hot plate, the substrate's backside is brushed over an acetone soaked paper to avoid that the sample is baked to the hot plate.

Cr deposition. In order to enhance the conductivity of the PMMA, a 10 nm Cr layer is deposited on the PMMA. This is necessary because the substrate is not conducting and a suitable conductance is necessary for the e-beam writing.

E-beam writing. For the e-beam writing a mask is designed with AutoCAD or similar programs. The e-beam writer VISTEC EBPG 5000 plus is used. Due to the electron beam polymers in the PMMA are cracked at positions that are exposed to the beam. These cracked polymers are subsequently removed with a special solution, the developer.

Cr etching and development of PMMA. To etch the Cr layer a special mixture is used, which consists of ceric ammonium nitrate, perchloric acid and water. With a Cr etching rate of about 80 nm/min⁶², the appropriate etching time is 12 s for our layer thickness. After that, the sample stays in propanol for 1 min. For the development, the sample is dried with nitrogen gas and immersed in the developer AR600-55 for 90 s. Now only the inversed pattern is left.

Ti/Pt deposition. For the metallic structure first Ti is deposited, as an adhesion layer, and on top Pt is deposited. Both metals are evaporated and cover the PMMA and the open areas. The thickness of the Ti-layer is 5 nm, the Pt-layer thickness is 15 nm or 25 nm.

Lift-off. To obtain the final structure, the PMMA with the Ti/Pt layer has to be removed (lift-off). This is done by placing the sample in acetone for 15 min in an ultrasonic bath. In the end the

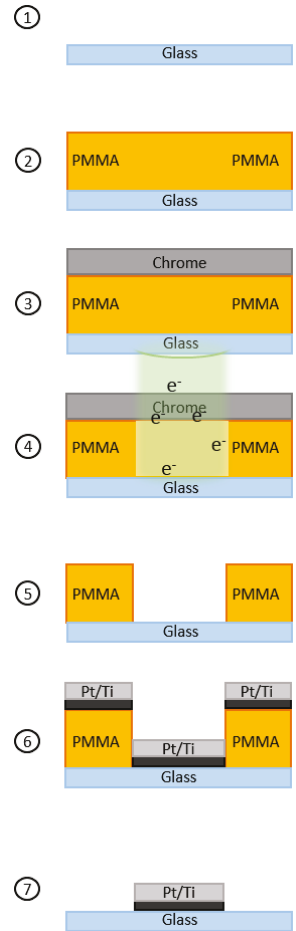


Figure 13. A schematic sketch of the different steps of the sensor preparation.

acetone is removed with propanol (3 min ultrasonic bath) and dried with nitrogen gas. Only the final structure is left over (Figure 12b-c).

III.4 Ex situ characterization methods

Additional to the in situ control and analysis via the capacitive sensor, ex situ characterization of the resulting film is of importance. The major methods used in this work are presented in this chapter.

- (i) In section III.4.1 we start with the general electronic characterization of molecules in the liquid state, which provides among others the permittivity of the investigated molecules.
- (ii) In section III.4.2 and III.4.3 followed description of the ellipsometry and water contact angle measurements, which are widely used techniques for the characterization of the quality of molecular layers.
- (iii) The streaming potential technique in section III.4.4 is used for the analysis of the electronic properties of the molecular layers.
- (iv) Atomic force microscopy in section III.4.5 is used for characterization of the surface morphology.
- (v) Finally, the fluorescence microscopy in section III.4.6 is used to visualize PLL+FITC and neurons on the surface of the samples.

III.4.1 Electronic measurement of molecules in the liquid state

For the electronic characterization of molecules in the liquid state, a simple electronic setup, which consist of a parallel plate capacitor encased in a PVC container (see Figure 14). The size of the electrodes and their spacing are $A = 10 \times 10 \text{ mm}^2$ and $s = 1 \text{ mm}$, respectively. In order to avoid any reaction (e.g. polymerization) of the molecules for instance due to humidity, the system is placed in a plastic housing, which is flooded with inert gas (N_2). After introducing the molecules with an injector between the electrodes, the conductivity σ and permittivity ε (see Figure 15) can be measured and evaluated:

$$\sigma = \frac{I}{U} \cdot \frac{s}{A} = \frac{U_m}{R_S(U_a - U_m)} \cdot \frac{s}{A}, \quad (8a)$$

$$\varepsilon_{liquid} \approx C_{liquid} \frac{s}{\varepsilon_0 A}, \quad (8b)$$

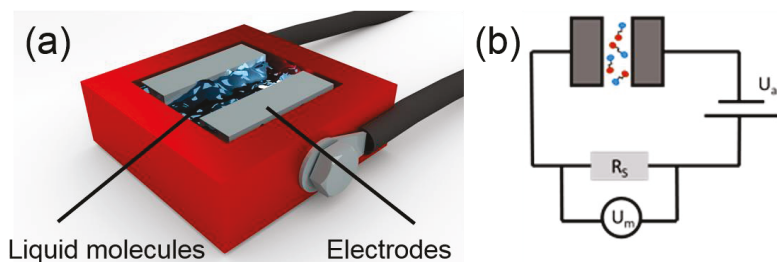


Figure 14. (a) Schematic sketch of the parallel plate setup for the capacitive measurement of electronic properties of molecules in the liquid state, and (b) electronic measuring principle.

where U_m is the measured voltage at the shunt R_s , U_a is the applied voltage, s is the spacing between the electrodes and A is the size of the electrodes, C_{liquid} is the capacitance of the molecules in the liquid state. Examples of measurements of molecules in the liquid state are given in Figure 15.

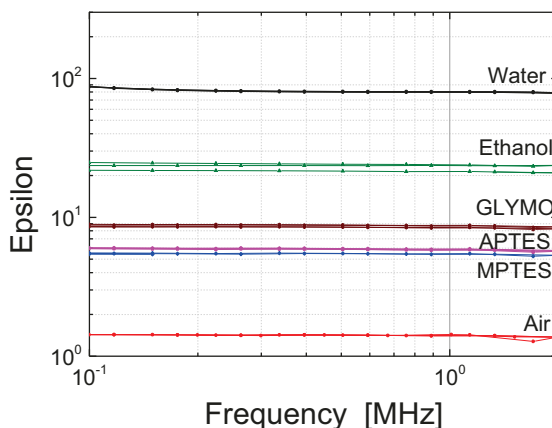


Figure 15. Frequency dependence of the permittivity of water, air, ethanol as references and molecules: APTES, GLYMO and MPTES measured with the parallel plate setup (see Figure 14).

III.4.2 Ellipsometry

Ellipsometry is a very sensitive optical method for determining either the refractive index or (if the refractive index is known) the thickness of a thin layer. We use this method to determine the

thickness of the molecular layer assuming that the refractive index of the layer is similar to that of SiO_2 . A schematic sketch of an ellipsometer is shown in Figure 16.

When an electromagnetic wave is incident on a medium, only part of it is transmitted into the medium. The fraction that is reflected post depends on the complex refractive index, the angle of incidence, and the polarization state of the wave. For layers with different complex refractive indices, the fraction also depends on the layer thicknesses.

The two basic types of polarization are parallel and perpendicular polarization. The orientation of the electric vector refers to the plane of incidence, which is defined by the directions of the incident and reflected waves. The (intensity-independent) ratios of the amplitudes and phases of the reflected and incident parallel and perpendicular polarized electric fields are described by the complex reflectances r_p and r_s , respectively. The complex reflectance ratio ρ of the system is then given by the ratio between r_p and r_s :

$$\rho = \frac{r_p}{r_s} = \tan(\Psi)e^{i\Delta}, \quad (9)$$

where $\tan(\Psi)$ is the ratio of the amplitude for reflection and Δ is the phase shift.

Since ellipsometry is measuring the ratio of two values (rather than the absolute value, it is a very robust, accurate, and reproducible method.

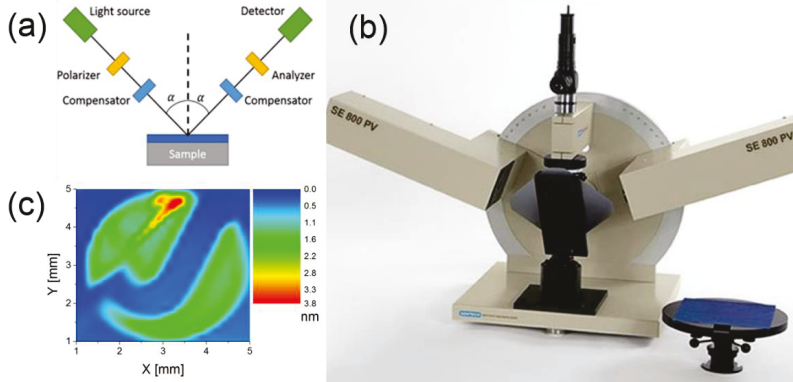


Figure 16. (a) Ellipsometry measurement principle. The laser light beam is polarized by a polarizer and hits the surface. After reflection from the sample surface, the beam passes through the analyzer in the detector. Typically, nowadays a CCD5 camera is used as a detector. (b) A photo of the SE 800 ellipsometer made by SENTECH Instruments GmbH. (c) Contour plot of the patterned Research Center Jülich logo made via APTES molecules determined via ellipsometry on SiO_2 -terminated Si substrate (size 10 mm x 10 mm).

However, ellipsometry is an indirect method, i.e. in general the measured values of Ψ and Δ cannot be converted directly into the optical constants or thickness of the layer. Direct inversion of Ψ and

Δ is only possible in very simple cases of isotropic, homogeneous and infinitely thick films. In all other cases a layer model is used, which considers either the optical constants (refractive index or dielectric constant) or the thickness of all individual layers of the sample including the correct layer sequence. Using an iterative procedure (least-squares minimization) unknown optical constants and/or thickness parameters can be varied, and Ψ and Δ values are evaluated using the Fresnel equations. The theoretical Ψ and Δ values, which match the experimental data best, provide either the optical constants or the thickness of the layer (or layer stack).

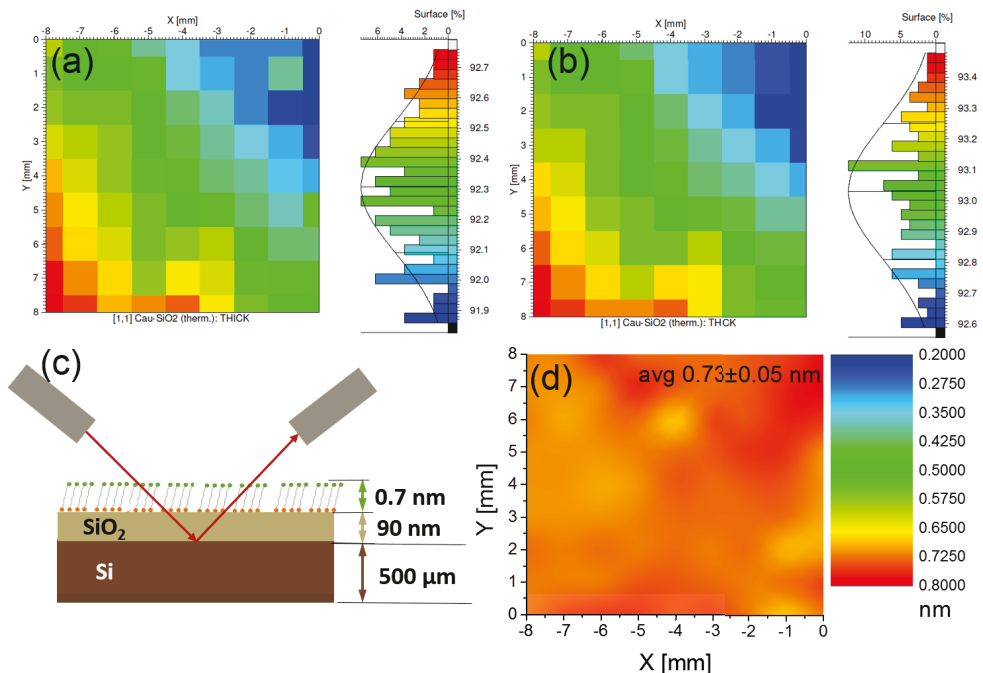


Figure 17. (a) 81 point measurement of SiO₂ terminate Si substrate without molecules before the deposition. (b) 81 point measurement of SiO₂ terminate Si substrate with molecules after the deposition. (c) Schematic measurement principle of the SiO₂ terminate Si with molecules and corresponding sizes of the substrate, SiO₂ layer and APTES molecules. (d) The resulting contour plot of the thickness of the APTES monolayer determined via ellipsometry on SiO₂-terminated Si substrates (size 10x10 mm²). The images are constructed from local measurements of every square millimeter of a regular 9 x 9 raster on the substrate before (a) and after (b) deposition. Average values and standard deviation are obtained from the resulting 81 data points.

In this case we usually start with a SiO₂ terminate Si wafer. In this case the thickness of the SiO₂ layer is typically ~90 nm and is measured before deposition of the molecular layer (see Figure 17a). By repeating the experiment after the deposition (see Figure 17b), and assuming that the additional molecular layer has similar optical properties as SiO₂ (actually $\epsilon_{opt}(SiO_2) \approx 3.9$, $\epsilon_{opt}(SAM) \approx$

4 – 8). We get a slight enhancement of the thickness of the layer after the deposition of the molecules. After subtracting the reference measurement the thickness of the molecular layer is obtained (see Figure 17d)

$$h_{mol} = h(SiO_2 + SAM) - h(SiO_2) \quad (10)$$

This is shown in Figure 16c for a patterned molecular layer showing the J-symbol of the research center Jülich.

III.4.3 Contact angle measurements

Contact angle measurements performed with OCA15EC measuring system (Figure 18b) are used in this work to determine the hydrophilicity (Figure 18c) (or hydrophobicity, see Figure 18d) of the surface which is a characteristic of the surface.

The contact angle Θ is the angle, defined by the liquid-vapor interface of a liquid drop on a solid surface (Figure 18a). It quantifies the wettability of a solid surface defined by the thermodynamic equilibrium of a given system consisting of solid, liquid, and vapor. As such the equilibrium contact angle reflects the relative strength of the liquid, solid, and vapor molecular interaction at a given temperature and pressure (in our case room temperature and atmosphere pressure). Thus, the shape of a liquid drop on the surface is effected by the surface free energy and is therefore suitable for measuring specific surface properties such as surface energy for instance.

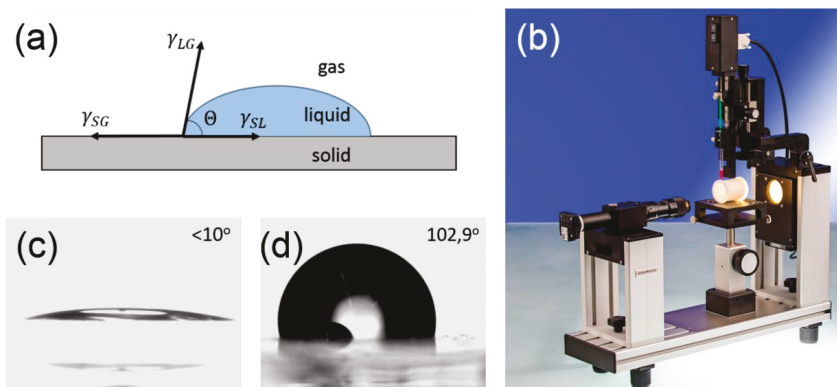


Figure 18. (a) Contact angle Θ of three-phase solid/liquid/gas system with interfacial energies γ_{SL} , γ_{SG} , γ_{LG} of solid/liquid, solid/gas and liquid/gas interfaces respectively. (b) Contact angle measuring system OCA15EC used in this work. (c) A water drop of 10 μ L on the hydrophilic surface. (d) A water drop of 10 μ L on the hydrophobic surface.

Using the solid-vapor interfacial energy γ_{SG} , the solid-liquid interfacial energy γ_{SL} and the liquid-vapor interface energy γ_{LG} , and assuming a perfectly planar surface, the equilibrium contact angle can be calculated using Young equation:

$$\cos(\Theta) = \frac{\gamma_{SG} - \gamma_{SL}}{\gamma_{LG}} \quad (11)$$

In case of $(\gamma_{SG} - \gamma_{SL})/\gamma_{LG}$ being larger than 1 this equation has no solution and the liquid would cover the complete surface. This is for instance the case for superfluid material. Usually $(\gamma_{SG} - \gamma_{SL})/\gamma_{LG}$ is smaller than 1, i.e. there exists a solution and thus a well-defined contact angle Θ . In case of water, a large water contact angle $\Theta > 90^\circ$ indicates a hydrophobic surface whereas a small contact angle $\Theta < 90^\circ$ is characteristic for a hydrophilic surface. The contact angle can also be used as a characteristic for a given SAM. For example, for APTES monolayers, the water contact angle depends on the type of monolayer and the monolayer coverage. Values ranging from 45° to 70° are represented in literature^{32,33}. However for a “proper” APTES SAM we expect a value of $\sim 60^\circ$ ⁶³. For other molecules other angles are measured. For example, for 1H,1H,2H,2H-Perfluorooctyltrichlorosilan (FOTCS) the typical contact angle is about 100° ³². Therefore, the contact angle can be used to identify “perfect” SAMs.

In our case the contact angle is determined via the “sessile drop method”. It is based on the investigation of the complete shape of a liquid drop lying on a planar solid surface. The image of the drop is captured with a camera and the contact angle is automatically recognized.

III.4.4 Surface potential measurement

In this work we used the streaming current method to determine the so-called ζ potential of our films which is correlated to the surface charge (Figure 19b).

Generally, solid surfaces in contact with a polar medium show definite surface charges caused by ionization, ionic adsorption, and ionic dissolution at the interface. These charges influence the neighboring ions in the polar medium. The rearrangement of the charges at the solid surface and the balancing charges in the medium are usually described by the electrical double layer (EDL) model.

The EDL consists of an immobile layer and a mobile layer (see Figure 19a). The redistribution of ions in the EDL generates the electrical potential (red line in Figure 19a) near the charged surface. The boundary between the immobile layer and the mobile layer is called the shear plane. The electrical potential at the solid surface is difficult to measure directly. However, the electrical potential at the shear plane, called ζ potential, can be measured and therefore represents a very important property of the solid-liquid interface. It is given by:

$$\zeta = \Psi(d^{ek}) . \quad (12a)$$

In the immobile layer the potential changes linearly with the distance x , whereas in the mobile layer it varies exponentially with x :

$$\Psi(x) = \Psi(d^{ek})e^{-\kappa(x-d^{ek})} . \quad (12b)$$

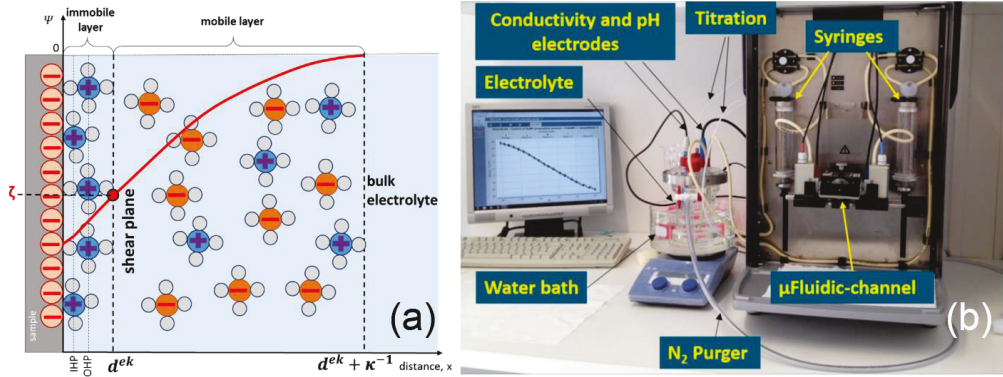


Figure 19. (a) Schematic sketch of the electrical double layer (EDL) according to the Gouy-Chapman-Stern-Grahame theory and (b) photo of the streaming current set-up (electrokinetic analyzer SurPASS).

In this work, a streaming current method is chosen for the determination of the ζ potential. In principle it consist of a microchannel formed by two parallel planar sample surfaces with channel height H , width W , cross section $A = H \times W$, and length L (Figure 20).

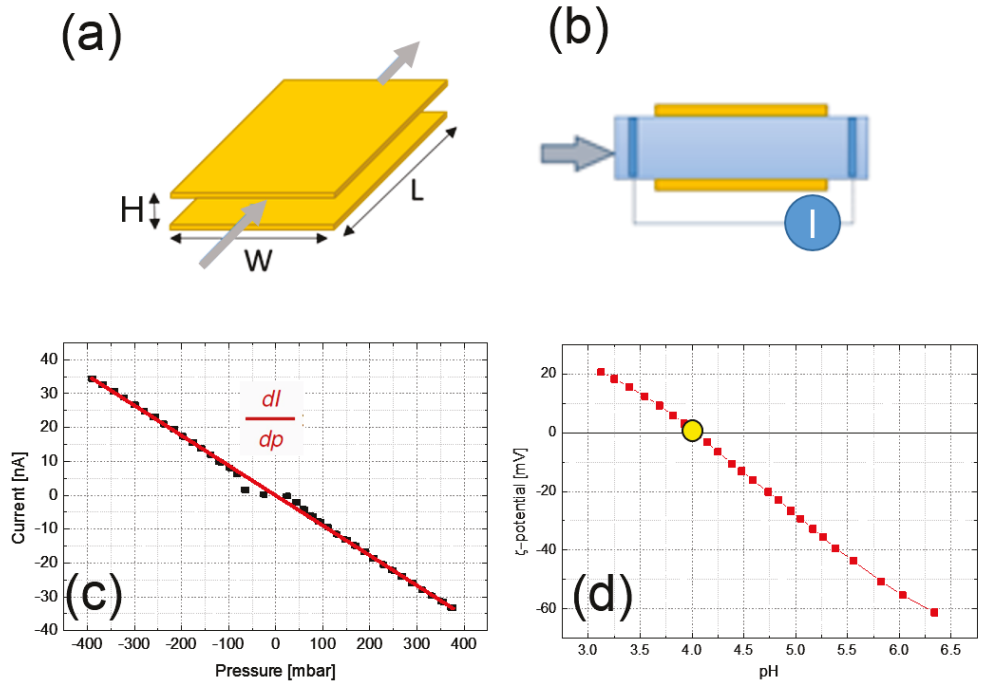


Figure 20. Parallel plate microchannel (a) for the streaming current measurements and sketch of the measurement principle (b). The gray arrows indicate the flow direction. Furthermore, an example of a streaming current measurement (c) and the resulting evaluations of the ζ potential (d) according to the eq.14.

When an electrolyte is forced to flow through the microchannel under an applied hydrostatic pressure Δp between the two ends of the microchannel, the counter ions in the mobile layer of the EDL are carried downstream resulting in an electric current in the pressure-driven flow direction. This current is known as the streaming current:

$$I_{str} = -\frac{\varepsilon\varepsilon_0\zeta A}{\eta L} \Delta p \quad , \quad (13)$$

with η and ε representing the dynamic viscosity and the relative dielectric constant of the liquid, respectively. The current I_{str} can be recorded with measuring electrodes at both ends of the capillary that are connected via a small external resistance (short-circuit conditions).

In order to analyze the surface potential of the molecular layer, we use a modified electrokinetic analyzer (SurPASS, AntonPaar Germany GmbH). A pair of identical planar substrates (10 mm \times 10 mm) is placed in a clamping cell with the surfaces to be analyzed facing each other and forming a microfluidic channel. In order to obtain a large signal, a small separation (typically $H \sim 100 \mu\text{m}$)

between the two plane-parallel surfaces is chosen that still allows a laminar flow of the electrolyte. The ζ potential is determined via a measurement of the pressure dependence of the current (Figure 20c) using the Smoluchowski equation, which follows Equation (11):

$$\zeta = \frac{dI}{dP} \frac{\eta L}{\varepsilon \varepsilon_0 A}, \quad (14)$$

where P is the pressure necessary to generate the laminae flow, η and ε are the viscosity and dielectric constant of the electrolyte, L and A represent the length and cross section of the flow channel, respectively, and I is the resulting current measured between two electrodes placed at each side of the measuring cell.⁵⁶ The resulting ζ potential represents the potential at the shear plane between the immobile (Helmholtz layer) and mobile layers and represents a measure for the surface potential.⁶⁴

III.4.5 AFM

Atomic force microscope (AFM) is used in this work to analyze the surface topography of our molecular layers, especially in case of patterned molecular layers. AFM represents a unique mechanical scanning technique of surfaces on nm-scale and is based on atomic forces (Figure 21b). Mounted on a cantilever, a tip is moved above the surface (Figure 21a). Due to the atomic interaction (force) between tip and surface, the tip's motion depends on the surface and is recorded using the reflection of a laser beam on the cantilever in a 2D position sensitive photodetector³². A typical example obtained from a patterned molecular layer is shown in Figure 21c. The AFM can measure in different modes. In the contact mode, the topography is scanned. With the tapping mode, the elasticity (in contact with the surface) or van der Waals force (without contact) is analyzed.

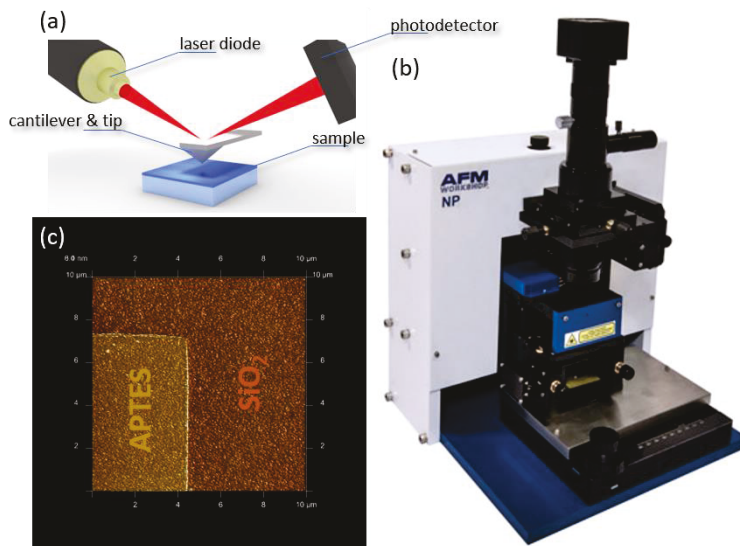


Figure 21. Sketch of the working principle (a), image of an AFM setup (b) (AFMWorkshop) and an example of a typical measurement of a patterned APTES layer on SiO_2 (c). The light part in (c) represents the area covered with molecules and the dark part the pure SiO_2 substrate.

With AFM, we can take a closer look at molecular layers that are deposited onto activated and non-activated SiO_2 . Figure 22a shows the topography of patterned (checkerboard pattern) APTES layer deposited onto an activated Si/SiO_2 substrate. For comparison, an AFM image of an identical APTES deposition however without ozone activation is shown in (c). The difference in the topography and the phase contrast between these two samples is evident:

- (i) the contrast (i.e. height difference for the topography (a, c) and different elasticity for the tapping mode (b, d) is larger for activate substrates and
- (ii) there are “white lines” marking the borders between the areas with and without APTES. It turns out that the white lines represent walls that consist of carbon, which stems from the resist, which is destroyed and locally redeposited during the ozone activation.

The histogram of the height profile in Figure 22 reveals the average thickness difference between the areas with and without APTES. For the activated sample, the distance between the peaks is approximately 1.59 nm, corresponding to approximately two layers of APTES⁴⁷. The large thickness of the APTES layer might be caused by redistribution of resist similar to the formation of the carbon walls separating fields with and without APTES. In case of the non-activated sample, the difference in height is 0.83 nm, which is close to the length of an APTES molecule. Figure 22 b and d indicate that the material is different for the areas covered with APTES and the SiO_2 areas.

This means AFM can be used to demonstrate the presence of molecule layers. However, the resulting thickness are questionable and moreover, this method is very time consuming and restricted to patterned samples.

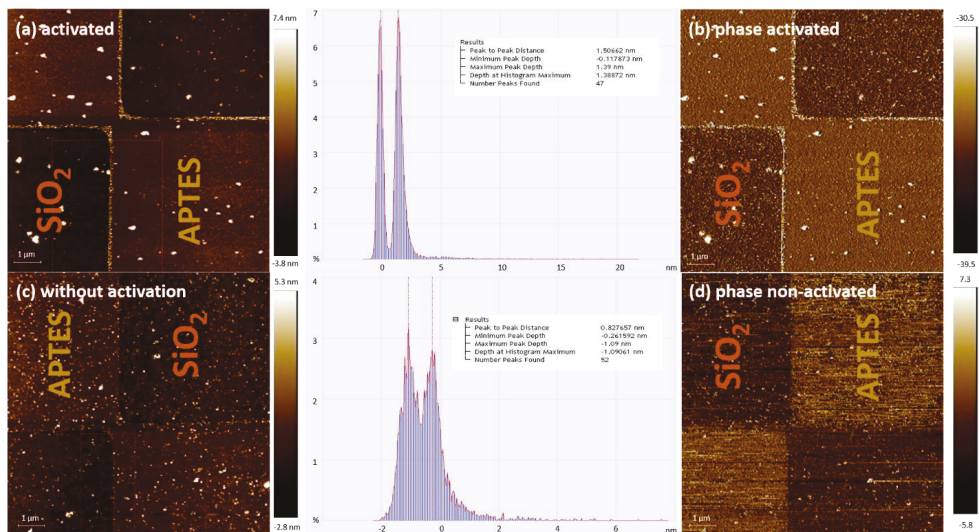


Figure 22. AFM data obtained for a patterned (checkerboard pattern) molecular (APTES) layer on activated (top) and non-activated (bottom) SiO₂ showing the topology (left), the resulting thickness distribution (middle), and the phase distribution (right).

III.4.6 Fluorescence microscopy

In this work fluorescence microscopy has been used for visual detection and analysis of

- (i) the protein (PLL) combined with fluorescent marker (FITC) on the substrates covered with mixed monolayers and
- (ii) live and dead neuronal cells modified with fluorescent dyes.

The absorption and subsequent emission of light by organic and inorganic specimens is typically the result of fluorescence or phosphorescence. Fluorescence describes the nearly simultaneous absorption and emission (delay usually less than a microsecond). Whereas emission persists longer after the excitation light has been extinguished in case of phosphorescence. The basic function of a fluorescence microscope is to irradiate the specimen with a desired and specific wavelength, and then to separate and collect the much weaker emitted fluorescence. In a properly configured microscope, only the light emitted from the sample should be detected so that the resulting fluorescent structures are superimposed with high contrast against a very dark (or black) background. The limits of detection are generally governed by the darkness of the background,

and the excitation light is typically several hundred thousand to a million times brighter than the emitted fluorescence.

The fluorophore emission (or absorption) intensity peak is usually lower in wavelength and magnitude than that exhibited by the excitation peak, and the emission spectral profile is often a mirror image (or nearly so) of the excitation curve, but shifted to longer wavelengths (see Figure 23a). The effective separation and detection of excitation and emission wavelengths is achieved in fluorescence microscopy through the proper selection of filters to block or pass specific wavelength bands in the ultraviolet, visible, and near-infrared spectral regions.

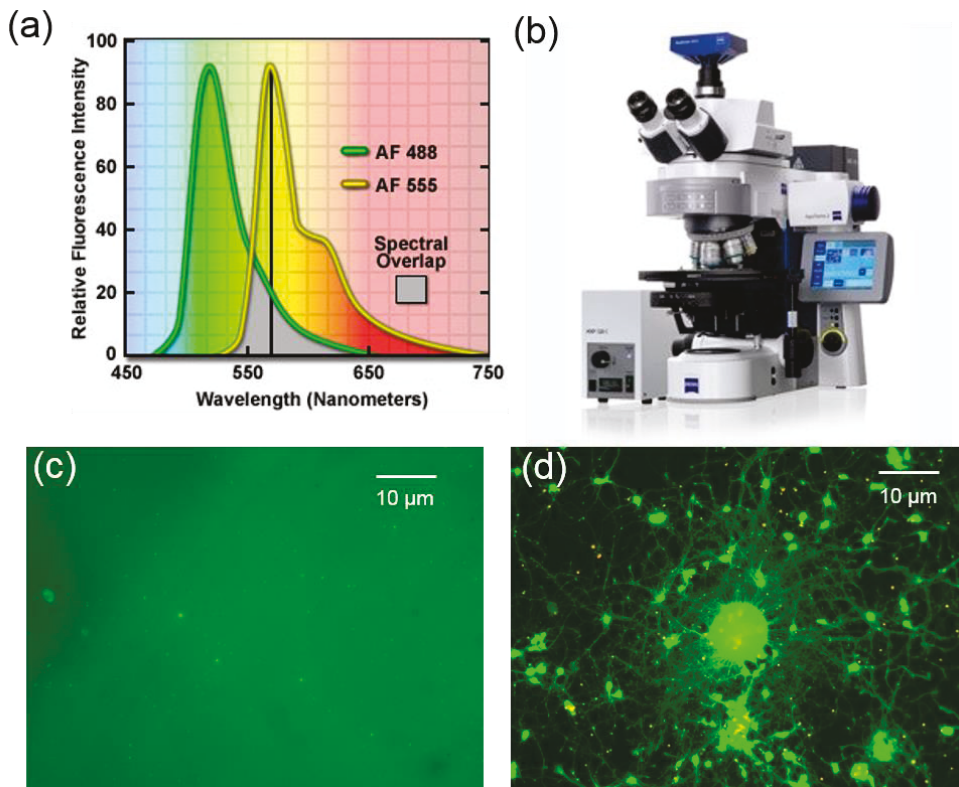


Figure 23. (a) Fluorophore emission profiles for 488nm (live cells) and 555nm (dead cells), (b) image of fluorescence microscope “ZEISS ApoTome”, and examples of fluorescence microscope images of a SiO₂ terminated Si substrate covered with molecules and PLL+FITC. (c) or covered by molecules, PLL+FITC and neurons (d).

In this work we used a Zeiss Apotome microscope (see Figure 23d) and Zen software. Usually, three images are taken from different areas of each sample with an exposure time of 600 ms and an illumination intensity of 3.04 V from a Zeiss HXP light source. In order to obtain representative

values for the intensity of fluorescence averaged intensities for areas of $30\ \mu\text{m} \times 30\ \mu\text{m}$ were taken using the software ImageJ.

In case of neurons (Figure 23d), we used $1\ \mu\text{g/ml}$ Calcein-AM and $2\ \mu\text{M}$ Ethidium Homodimer (both Life Technologies) in supplemented cell growth medium to stain live and dead cells in green and red, respectively. After the staining the cell statistics was performed via using the software ImageJ as well.

III.5 Cell culturing

In this work we use different biological objects in order to demonstrate biocompatibility and “bioengineering” of mixed molecular monolayers. The necessary techniques are described in this chapter.

III.5.1 PLL preparation

Polylysine (PLL) is a synthetic polymer, a homopeptide commonly used to coat tissue cultureware as an attachment factor that improves cell adhesion. Fluorescein isothiocyanate (FITC) is an original fluorescein molecule functionalized with an isothiocyanate reactive group, replacing a hydrogen atom on the bottom ring of the structure. This derivative is reactive towards nucleophiles including amine and sulfhydryl groups on proteins. In order to visualize the PLL coating via fluorescence microscopy (see chapter III.4.6) we used a PLL+FITC solution. This PLL+FITC (P3069, Sigma-Aldrich) solution was mixed with Gey's Balanced Salt Solution (GBSS, Sigma-Aldrich) to a final concentration of $10\ \mu\text{g/mL}$ (i.e. $1\ \mu\text{g}$ of PLL+FITC mixed in $100\ \mu\text{L}$ of GBSS). The samples were coated with a drop ($45\ \mu\text{l}$) of the solution and kept at room temperature for 1 hour avoiding any exposure to light. The remaining drop was then removed from the surface by rinsing with pure GBSS and washing away the residual protein that had not bonded to the SAM. The sample was subsequently rinsed in the Milli-Q water for 5 minutes and purged in a N_2 flow. After the entire process was complete, the adhesion of the PLL to the carries (e.g. coated with mixed molecular layer) can be visualized via fluorescence microscopy.

III.5.2 Neuronal culture

Cortical neurons were obtained from E18 Wistar rat embryos. Briefly, cortex was dissected from the embryonic brain tissue and digested with trypsin-EDTA at 37°C , $5\%\ \text{CO}_2$, 100% humidity for 15 min. In order to remove trypsin, the cortex was washed 5 times with Neurobasal medium (Life Technologies GmbH, Germany) supplemented with 1% B27 (Life Technologies, Germany), $0.5\ \text{mM}$ L-glutamine, and $50\ \mu\text{g/mL}$ gentamicin. Then the cortex was dissociated gently with a $1\ \text{mL}$ pipette. Cell clumps were allowed to settle for 2 min at room temperature. The supernatant was

diluted in supplemented neurobasal medium and cells were plated at $\sim 20\text{k cells/cm}^2$. Medium was changed completely 4 hours after plating. In the following days the medium was half changed twice per week. The animal work was carried out with approval of the Landesumweltamt für Natur, Umwelt und Verbraucherschutz Nordrhein-Westfalen, Recklinghausen, Germany, number 84-02.04.2015.A173

III.5.3 HL-1 cell culture

The cardiomyocyte-like cell line HL-1 was cultured in T25 flasks. Prior to seeding on MEAs, the chips were cleaned with 70% ethanol and coated with fibronectin ($5\ \mu\text{g/mL}$). When reaching 100% confluency, the cells were passaged and seeded on top of the MEAs at 10k cells per chip. The chips were then placed in an incubator ($37\ \text{°C}$ and 5% CO_2) for the cells to mature. Claycomb medium, supplemented with 10% fetal bovine serum, 100U/ml-100 $\mu\text{g/ml}$ penicillin-streptomycin, 0.1mM norepinephrine and 2 mM L-glutamine was exchanged every day (100%) and two hours before the measurements.

III.5.4 Live-dead imaging

Live-dead staining was performed using $1\ \mu\text{g/ml}$ Calcein-AM and $2\ \mu\text{M}$ ethidium homodimer (both Life Technologies) in supplemented cell growth medium to stain live and dead cells in green and red, respectively. Cells and dyes were incubated for 15 minutes in a $37\ \text{°C}$ incubator or on a $37\ \text{°C}$ hot plate (if performed after the electrical measurements). The samples were observed via a Zeiss Apotome microscope using Zen software. 3 positions for each condition (the protein treated area, the untreated SAM, and the border between these two regions) were imaged in 2 separate cultures.

IV. Results and discussion

In this section we present and discuss the experimental results of this work. This is done in three steps:

- (i) first, in chapter IV.1, we start with the description of the novel in situ controlled molecular layer deposition,
- (ii) then, in chapter IV.2, we move to more complex layers, i.e. mixed SAMs, and thus demonstrate the engineering of the surface properties, and
- (iii) finally, in chapter IV.3, we demonstrate the potential of the mixed molecular layers for bioelectronics applications.

IV.1 In situ analysis of the growth and dielectric properties of organic SAMs

Organic nanoscale science and technology relies on the control of phenomena occurring at the molecular level. This is of particular importance for the self-assembly of molecular monolayers (SAM) that can be used in various applications ranging from organic electronics to bioelectronic applications. However, the understanding of the elementary nanoscopic processes in molecular film growth is still in its infancy.

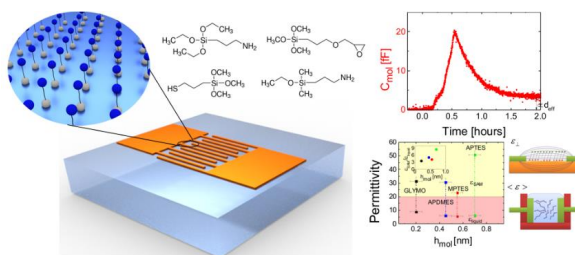


Figure 24. Schematic sketch of the highlights of this section IV.1 consisting of a novel in situ sensor for the controlled molecular layer deposition, the demonstration of the sensor and the resulting large permittivity of optimized SAMs.

In this chapter we describe a novel in situ and extremely sensitive detection method for the analysis of the electronic properties of molecular layer during molecular layer deposition. This low-frequency sensor (1 kHz) is employed to analyze the standard vapor deposition process of SAMs of molecules and, subsequently, it is used to optimize the growth process itself. By combining this method with an ex situ determination of the effective thickness of the resulting layers via ellipsometry, we observe a large difference of the permittivity of the examined aminosilanes in the liquid state ($\epsilon_{\text{liquid}} = 5.5\text{--}8.8$) and in SAMs ($\epsilon_{\text{SAM}} = 22\text{--}51$, electric field in the plane of the layer). We ascribe this difference to either the different orientation and order of the molecules, the different density of molecules, or a combination of both effects. Our novel in situ analyses not only allows monitoring and optimizing the deposition of organic layers but also demonstrates the high potential of organic SAMs as organic high-k layers in electronic devices.

IV.1.1 In situ controlled SAM deposition

Let us start with a standard molecular layer deposition (MLD). For this we use the GLOBUS system that was introduced in chapter III.2.2. The actual deposition takes place after activation of the surface of the substrate (using ozone) and establishing the deposition conditions, i.e. a given N_2 pressure in the recipient. By opening the source, the molecular deposition starts and can be monitored using the capacitive in situ sensor.

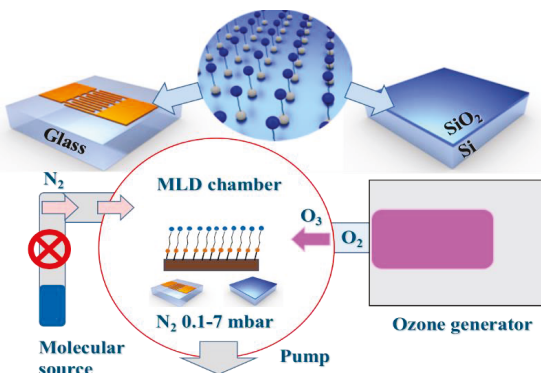


Figure 26a shows the molecular contribution C_{mol} to the capacitance for “standard” APTES deposition processes that are performed at different N_2 gas pressures (7, 5, 1, and 0.1 mbar). In these standard processes⁵⁶ a given process pressure is established and stabilized before the molecular source is opened and deposition sets in. Generally, the valve is opened at time defined as $t = 0$ (see Figure 26). The deposition rate strongly depends on the vapor pressure of the molecules which is related to the process pressure. For “standard” deposition of APTES we typically use a process pressure of 0.1–7 mbar. After deposition, the valve of the molecule source is closed and the recipient is pumped down to 10^{-4} mbar to remove excess molecules from the sample and the recipient. Finally, the layer thickness of all films is measured via ellipsometry. In all cases the layer thickness agrees with the value reported for SAMs of APTES in the literature,⁴⁷ that is, $h_{mol} \approx 0.7$ nm.

Figure 25. Schematic of the MLD setup and molecular layer deposition on the sensor (glass substrate with IDE) and SiO_2 terminate Si substrate.

In a next step we analyze the layer thickness during the deposition in a series of experiments in which the deposition is stopped at different times and the thickness of the molecular layer on the reference sample is measured via ellipsometry after each of these depositions. Figure 26b suggests that the thickness measured via ellipsometry seems to agree with the in situ measured capacitance changes. This indicates that in this standard process the SAM is gradually formed with the increase of the thickness of the molecular layer and that the SAM is finally accomplished when the thickness of the molecular layer saturates. This already tells us a lot about the SAM formation; however, it demonstrates two problems:

- (i) Why does the capacitance C_{mol} saturate at different values for different pressures, although we finally obtain monolayers with ~ 0.7 nm thickness in all cases, and
- (ii) inserting $h_{mol} = 0.7$ nm into Equation 6a would yield different and unrealistically large values for the permittivity of the molecule (e.g., $\epsilon_{mol} \approx 190$ and $\epsilon_{mol} \approx 120$ for 0.1 and 5

mbar, respectively). Therefore, we examined the deposition process and the permittivity of the molecules in more detail.

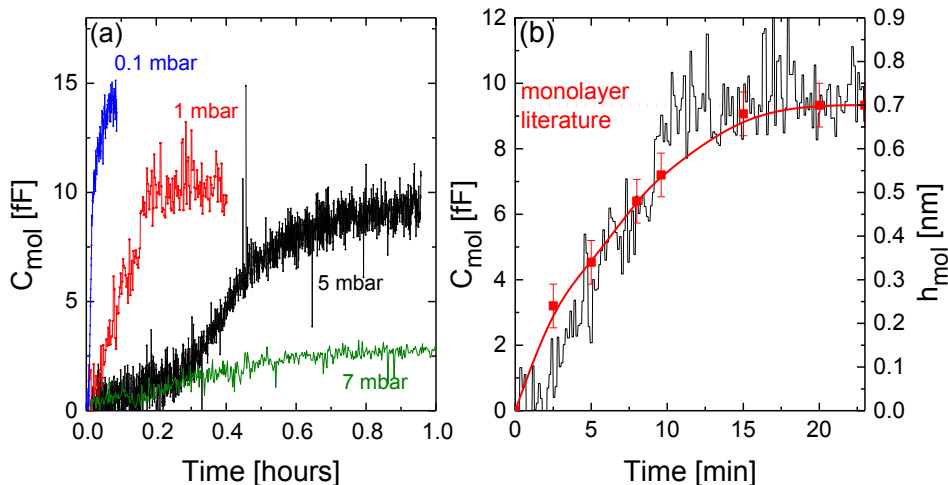


Figure 26. (a) Capacitance of molecular layers of APTES as function of time for 7, 5, 1, and 0.1 mbar N_2 work pressure and (b) comparison of the capacitive contribution C_{mol} and ex-situ measured (ellipsometry) effective thickness of the APTES layer for the deposition at 1 mbar. Additionally the literature value for a monolayer of APTES is indicated in (b).

For this we modified the deposition procedure by introducing a pressure profile (see Figure 27). To avoid the instability of the process when opening the valve of the molecule source, we started and terminated the actual deposition by opening and closing the valve of the molecular source at a high pressure (here, 18 mbar N_2) at which no evaporation of molecules is possible. For the actual deposition the N_2 pressure is reduced, and furthermore, the development of the layer is monitored even after deposition to observe the complete formation of the layer.

In detail:

- after opening the valve (no. 1 in Figure 27, time $t = 0$) there is only a small pressure peak due to the pressure difference between the molecule source and recipient, but no deposition as indicated by the stable capacitive signal of the sensor ($C_{mol} = 0$).
- After ~ 2 min of stabilization, the N_2 pressure is continuously decreased. At ~ 8 mbar (no. 2 in Figure 27) evaporation sets in and is detected in the form of an increase of the capacitance of the sensor. With decreasing pressure the molecule vapor pressure increases. The increase of the capacitance indicates that the film thickness also increases.
- After 30 min a N_2 pressure of ~ 0.5 mbar is reached and according to the sensor signal the molecular layer is already quite thick. Here, we start to increase the N_2 pressure again (no.

4 in Figure 27). Simultaneously, the capacitance starts to decrease, which indicates that with increasing pressure (decreasing molecular vapor pressure) the desorption dominates the adsorption of the molecules at the sensor.

- At high pressure (no. 5 in Figure 27) the valve of the molecule source is closed and N₂ gas is continuously pumped out.
- Finally, the N₂ flow is stopped (no. 6 in Figure 27) and the pressure drops to the background pressure of $\sim 1.5 \times 10^{-3}$ mbar. The capacitance decreases continuously during this process of pressure reduction and finally saturation at ~ 3.7 fF (no. 7 in Figure 27).

The modified deposition process recorded in Figure 25 shows a number of interesting features:

(i) The deposition (no. 2 in Figure 25) starts at ~ 8 mbar, which agrees with the maximum pressure at which APTES molecules vaporize, given in the literature.^{49,65,66}

(ii) With decreasing pressure the thickness of the molecular layer increases. It might be accidental, however, there are two different behaviors visible. In the first part (no. 2–3 in Figure 27) the increase is more “noisy” and shows a different slope compared to the second part (no. 3–4 in Figure 27). The transition from the first part to the second part (no. 3 of Figure 27) occurs at a value C_{mol} that seems to agree with the final values obtained after deposition (no. 7 of Figure 27) which represents the value obtained for a single molecular layer. Therefore, it might be that the first part (no. 2–3 of Figure 27) represents the formation of the SAM, whereas the second part (no. 3–4 of Figure 27) represents the deposition of additional molecules onto the SAM. These molecules have to be removed after deposition.

(iii) Once the SAM is formed (no. 3 in Figure 27), adsorption dominates desorption for decreasing pressure and vice versa for increasing pressure.

(iv) After deposition (no. 4 in Figure 27) additional molecules are removed from the SAM. This process can take a long time (here about 1.5 h).

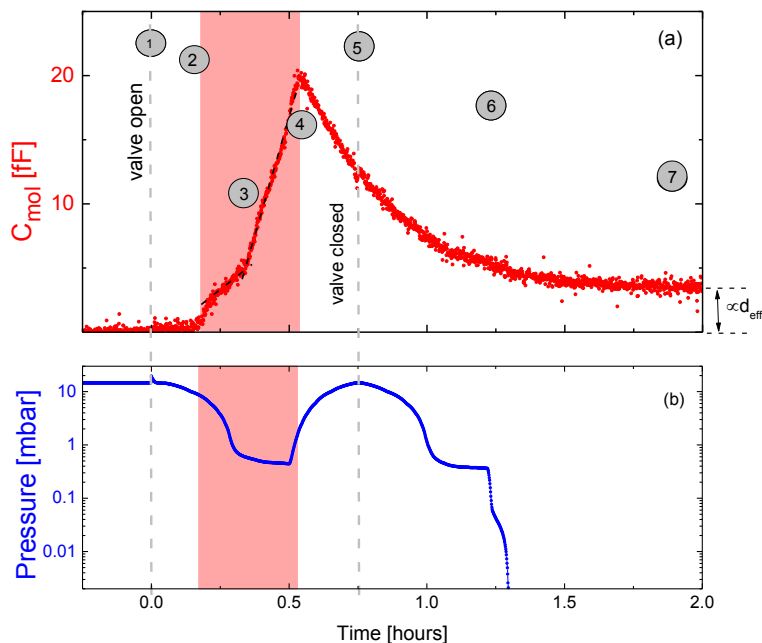


Figure 27. Molecular contribution to the capacitive signal (a) for a deposition process for APTES using a modified N_2 pressure profile (b). The different numbers represent the opening of the valve of the molecular source (1), the onset of deposition (2), the change of the deposition characteristic (most likely due to completion of the SAM) (3), the increase of the N_2 pressure profile (4), the closing of the molecular source (5), the closing of the N_2 flow (6), and the saturation of the capacitive signal (7).

(v) Finally (no. 7 in Figure 27), the capacitance contribution C_{mol} saturates, indicating that a stable molecular layer is formed. The thickness of the layer measured via ellipsometry is $h_{\text{mol}} \approx 0.7$ nm; that is, it agrees with the literature value for SAMs of APTES. From this we conclude that we deposited a SAM of APTES. However, the capacitive signal leads to a permittivity of the SAM of $\epsilon_{\text{SAM}} \approx 51$, which is much larger than the values $\epsilon_{\text{liquid}} \approx 6$ for APTES in the liquid state (see chapter III.4.1). This will be discussed in detail in the following.

IV.1.2 Dielectric properties of SAMs

For comparison, we performed similar experiments for the other molecules given in Table 1. Similarly to APTES, we obtained quite large values for the permittivity ϵ_{SAM} of the different molecules. The data are given in Table 1 and Figure 28. To compare the permittivity ϵ_{SAM} with the permittivity ϵ_{liquid} of the molecules in the liquid state, measured the permittivity of the molecules in the liquid state using the parallel plate device introduces in chapter III.4.1. The resulting permittivity ϵ_{liquid} ranges between 5.5 and 8.8 (see Table 1 and Figure 28). The comparison of the permittivity obtained for the molecules in the liquid state and the SAMs (electric field in the plane of the layer) shows that the values for ϵ_{SAM} are typically 4–9 times larger than ϵ_{liquid} for the same type of molecule (see inset of Figure 28). There are mainly two reasonable explanations for the large difference of the permittivity of the molecules in the different phases:

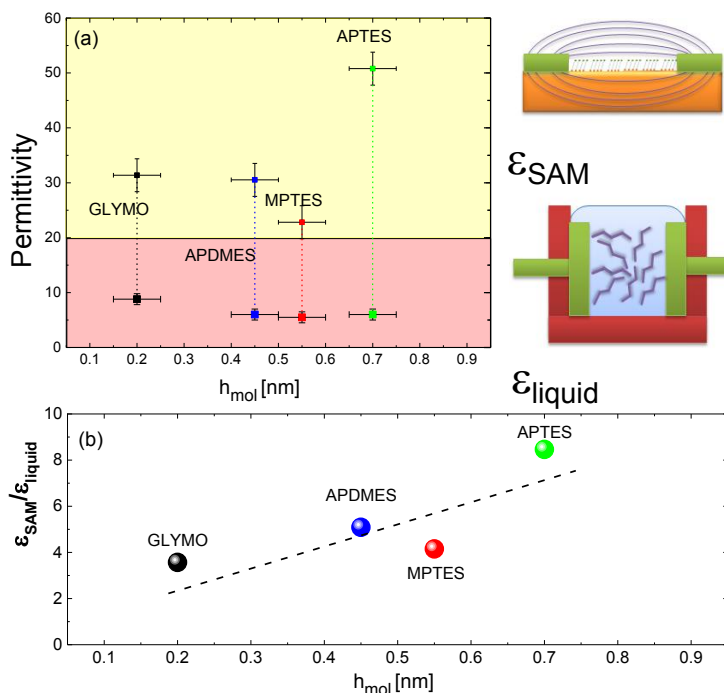


Figure 28. (a) Comparison of the permittivity of molecules in SAMs (upper symbols) and in the liquid state (lower symbols) as a function of the thickness of the SAM layer. The permittivities ϵ_{SAM} and ϵ_{liquid} are evaluated from the capacitive measurements on SAMs (electric field in the plane of the layer) using the layer thickness h_{mol} determined via ellipsometry and a parallel plate capacitor, respectively. The difference measurements are sketched. (b) Resulting ratio of the permittivity in the SAM and liquid state.

- First, complex molecules are known to be birefringent,⁶⁷ which automatically implies that their permittivity is anisotropic. Because of their structure, the molecules which are used in this work should also possess anisotropic permittivity. Consequently, they should automatically show different permittivity in SAMs and in the liquid state. In SAMs molecules are orientated, in the ideal case, normal to the substrate surface or slightly tilted, whereas in the liquid state there exist no well-defined orientation of the molecules.
- Second, it is known that SAMs with different density of molecules can be obtained via different deposition techniques.⁶⁸ Consequently, not only the orientation but also the density of molecules in SAM and liquid state differs appreciably. Both effects will have an impact on the electronic characteristics.⁶⁹ From this we can conclude that the permittivity of the dense state (SAM) can be larger than the permittivity of the less dense state (liquid). This is what we observe in the experiments for all molecules that were examined.
- Most likely, both of these explanations (i.e., anisotropic permittivity and different molecular density) are responsible for the large difference in the permittivities ϵ_{liquid} and ϵ_{SAM} .

IV.2 Controlled engineering of oxide surfaces for bioelectronics applications using organic mixed monolayers

Modifying the surfaces of oxides using self-assembled monolayers offers an exciting possibility to tailor their surface properties for various applications ranging from organic electronics to bioelectronics applications. The simultaneous use of different molecules in particular can extend this approach since the surface properties can be tuned via the ratio of the chosen molecules. This requires the composition and quality of the monolayers to be controlled on an organic level – i.e. on the nanoscale.

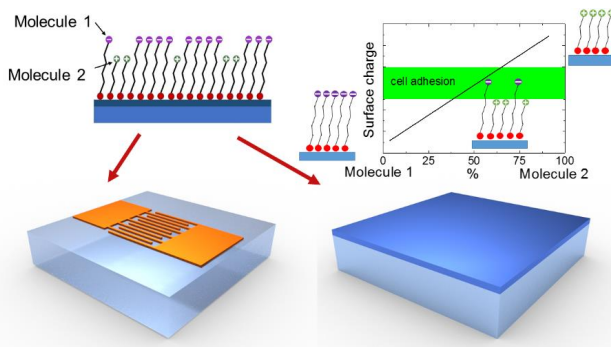


Figure 29. Sketch illustrating the strategy of the work in this chapter IV.2. SAM consisting of two different molecules with different functional groups (here positively and negatively charged) are deposited on the novel in situ sensor for the in situ control and analysis, and on substrates for extensive ex situ analysis (ellipsometry, wetting angle analysis, and surface potential measurements). The precise control of the ratio of the different molecules allows the tuning of surface properties (e.g. surface charge) for various applications (e.g. improved cell adhesion).

In this chapter, we present a method of modifying the surface and surface properties of silicon oxide by growing self-assembled monolayers comprising various compositions of two different

molecules – (3-aminopropyl)-triethoxysilane (APTES) and (3-glycidyoxypropyl)-trimethoxysilane (GLYMO) – by means of in situ controlled gas-phase MLD. The properties of the resulting mixed molecular monolayers (e.g. effective thickness, hydrophobicity, and surface potential) exhibit a perfect linear dependence on the composition of the molecular layer. Finally, coating the mixed layer with poly(L-lysine) (PLL) proves that the density of proteins can be controlled by the composition as well. This indicates that the method might be an ideal way to optimize inorganic surfaces for bioelectronics applications.

IV.2.1 Deposition of mixed molecular monolayers

In this section we describe the deposition of mixed molecular monolayers from the gas phase. The process is based on the knowledge obtained from the deposition of single molecular monolayers described in chapter IV.1. However this time we deposited two different molecules (first APTES, then GLYMO) using the two sources of the MLD device GLOBUS (see Figure 10). Again the use of the capacitive in situ sensor turns out to be extremely helpful.

Figure 30 presents typical examples of the deposition of a “pure” monolayer (Figure 30a) and a mixed monolayer (Figure 30b). It shows a combination of the signal C_{mol} of the capacitive sensor during deposition, the image of the resulting ellipsometry data, and illustrations which depict the deposition at different states of the process. The deposition process for the pure monolayer of APTES in Figure 30A is described in the following:

(i) Prior to the deposition process, the MLD chamber was evacuated and then filled with pure oxygen gas (99.9 %). At a pressure of 1 mbar, a microwave discharge produced ozone in the ozone generator (see Figure 10) which flowed through the deposition chamber and led to the cleaning (removal of molecules) and activation of the surface of the sample substrates and the sensor. This in situ activation represents an important first step for the following silanization processes.^{55,56}

(ii) Oxygen was removed (10⁻⁶ mbar) and, subsequently, a N₂ pressure (here 0.1 mbar) established in the recipient. At this point, the substrate surface was cleaned and activated, and the capacitive signal of the in situ sensor corresponded to the reference value without molecules, i.e. $C_{mol} \approx 0$.

(iii) When the molecule source (here APTES) was opened at time $t=0$, the deposition started and molecules were adsorbed at the surface of the sample substrates and the sensor. As a result, there was a sharp increase in the capacitive signal. From previous studies⁵⁷, we know that – depending on the pressure and deposition time – relatively thick molecular layers can be formed and that monolayers are not automatically obtained. At the chosen pressure (here 0.1 mbar) and time (here 10 min), we assume a rather thick multilayer of APTES.

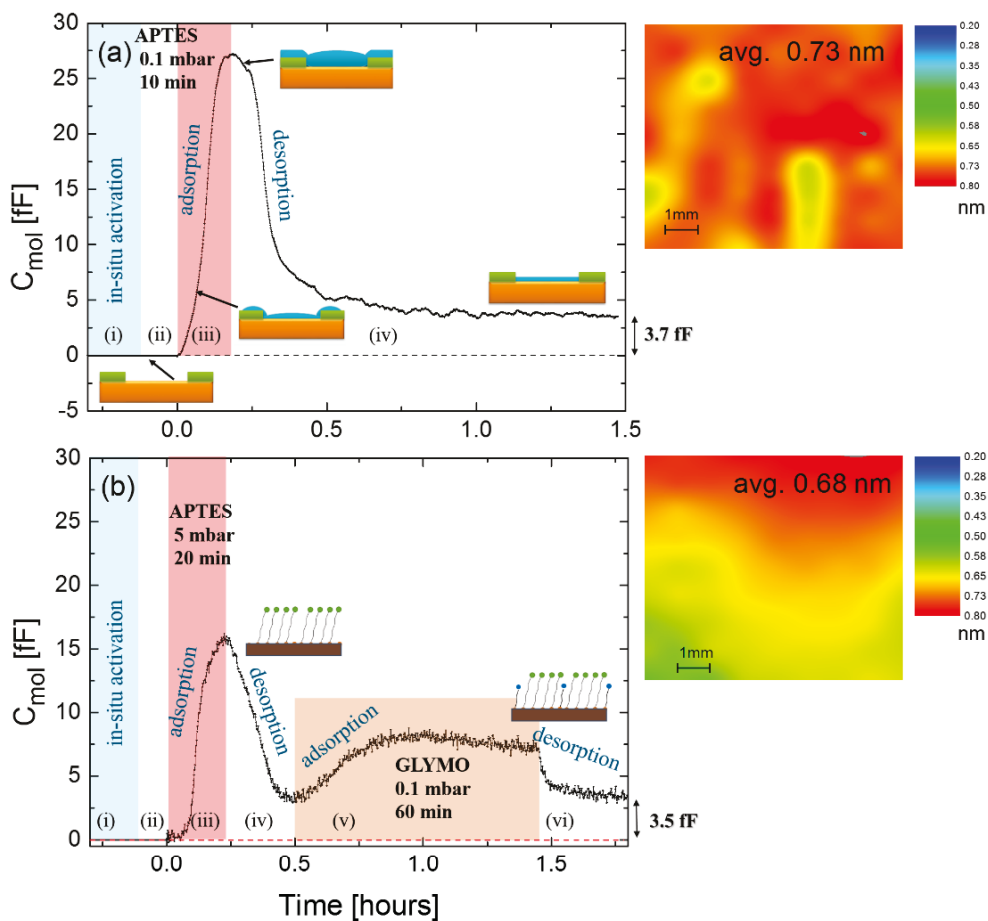


Figure 30. Capacitive signal of the molecular layers during the growth of (a) APTES and (b) a mixed layer obtained via successive deposition of APTES (5 mbar N_2 , 20 min) and GLYMO (0.1 mbar N_2 , 60 min). The different colors represent the different deposition steps: activation of the surface ((i), light blue), evacuating ((ii), white), deposition of APTES ((iii), red), deposition and removal of excessive APTES molecules ((vi), white), deposition of GLYMO ((v), orange), and desorption and removal of excessive GLYMO molecules ((vi), white). The different steps are described in detail in this paper. Additionally, final values are given for C_{mol} (they represent the capacitive contribution C_{SAM} of a SAM) and the contour plots of the thickness (including the average value), obtained via ellipsometry of the resulting molecular layers. The small diagrams illustrate the different deposition steps, the colors represent substrate (orange), electrodes (green), and molecular layer (blue).

(iv) After a given time (here 10 min), the molecular source was closed and desorption (i.e. removal of the additional molecules that are physisorbed at the surfaces of the substrates and the sensor) set in. This resulted in a strong decrease of the signal of the capacitive sensor. Finally, after about an hour, the C_{mol} signal stabilized, indicating that the molecular layer no longer changed. The resulting layer was then analyzed via ellipsometry. The average thickness of ~ 0.73 nm (see inset Figure 30a) and the surface properties (discussed later) indicate that a perfect monolayer of APTES was finally obtained. Thus, the process shown in Figure 30a depicts the deposition of a complete monolayer consisting of only one molecule, APTES. The final value of the capacitance C_{mol} represents the capacitive contribution C_{SAM} of a self-assembled monolayer.⁵⁷ The deposition of a monolayer of GLYMO is very similar, as it results in an average ellipsometry signal of 0.31 nm (see also Figure 30a)⁵⁷.

The deposition of mixed monolayers is slightly more complex (see Figure 30b). The first steps ((i) to (iv)) are identical to the process described above. However, for mixed layers we chose combinations of deposition time and pressure that do not allow the deposition of a complete monolayer. In the example in Figure 30b, a considerably larger pressure (5 mbar, resulting in a small APTES vapor pressure) and a deposition time of 20 min were chosen. The resulting maximum of the capacitive signal is smaller than that observed in Figure 30a and after deposition the signal rapidly decreased to relatively small values, thus indicating a deposition of an incomplete monolayer. After the first rapid decrease of the capacitive signal, which indicates the desorption of the additional physisorbed APTES molecules, the deposition process of the GLYMO was started:

(v) similar to step (iii), after stabilizing a N_2 pressure of 0.1 mbar, the GLYMO source was opened and GLYMO molecules adsorbed at the sensor and the substrates. As a result, the capacitive signal increased. In order to ensure complete coverage of the surface with GLYMO, the deposition was continued for 1 hour.

(vi) after 1 hour, the GLYMO source was closed. Additional physisorbed molecules were desorbed, which resulted in a decrease of the capacitive signal. Finally, the C_{mol} signal saturated at a value of ~ 3.5 pF, which is slightly smaller than the value of 3.7 pF obtained for pure APTES after saturation (Figure 30a). In addition, the resulting thickness of the molecular layer, which is obtained via ellipsometry, proved to be slightly smaller than that measured for pure APTES. The average thickness was 0.68 nm for this mixed APTES–GLYMO layer (see inset Figure 30b).

As a result, we obtained a monolayer which seems to consist of both types of molecules, APTES and GLYMO.

In order to vary the composition of the molecular layer, we simply varied the deposition time and N_2 pressure for the APTES deposition. The resulting thickness of the layers is summarized in Figure 31 and Figure 32.

Figure 31 presents typical examples of ellipsometry data for mixed layers obtained for different deposition parameters (APTES deposition time and pressure). The contour plots show that

- (i) the thickness of the resulting layers is quite homogeneous (± 0.045 nm) and that
- (ii) film thicknesses ranging from (0.31 ± 0.04) nm for pure GLYMO to (0.73 ± 0.04) nm for pure APTES can be established via this method.

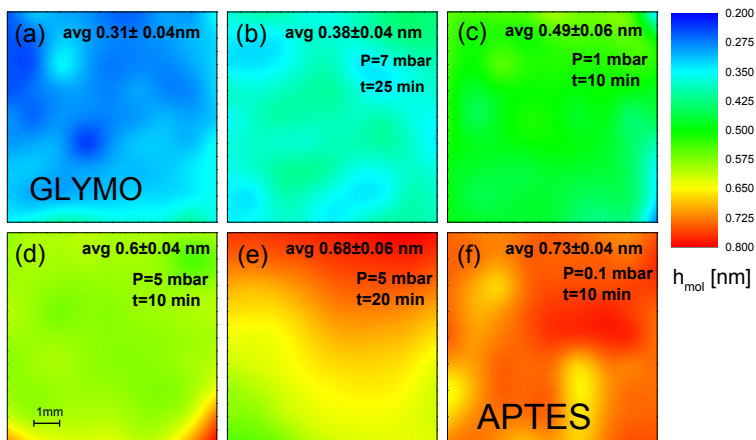


Figure 31. Contour plot of the thickness of the mixed molecular monolayer determined via ellipsometry on SiO_2 -terminated Si substrates (size 10×10 mm²). The images is constructed from local measurements of every square millimeter of a regular 9×9 raster on the substrate. Average values and standard deviation are obtained from the resulting 81 data points. The deposition parameters (deposition time and N_2 pressure during APTES deposition) and the average thickness values are added in detail. (a) pure GLYMO monolayer; (b)-(e) mixed APTES-GLYMO monolayers with different times t (given) and (f) deposition of pure APTES monolayer.

Figure 32 shows the dependence of the effective thickness of mixed APTES and GLYMO monolayers as a function of APTES deposition time for the different deposition pressures (0.1, 5, and 7 mbar). All depositions follow the exact procedure shown in Figure 30b, i.e. an initial brief deposition of a submonolayer of APTES is followed by an extended (1h at 0.1 mbar) deposition of GLYMO; only the deposition time and pressure for the APTES deposition is varied. All thickness values range between h_{mol} obtained for complete monolayers of GLYMO ((0.31 ± 0.04) nm) and APTES ((0.73 ± 0.04) nm)⁴⁷. The dashed lines in Figure 32 indicate the

dependence of the layer thickness on the APTES deposition time for the different deposition pressures.

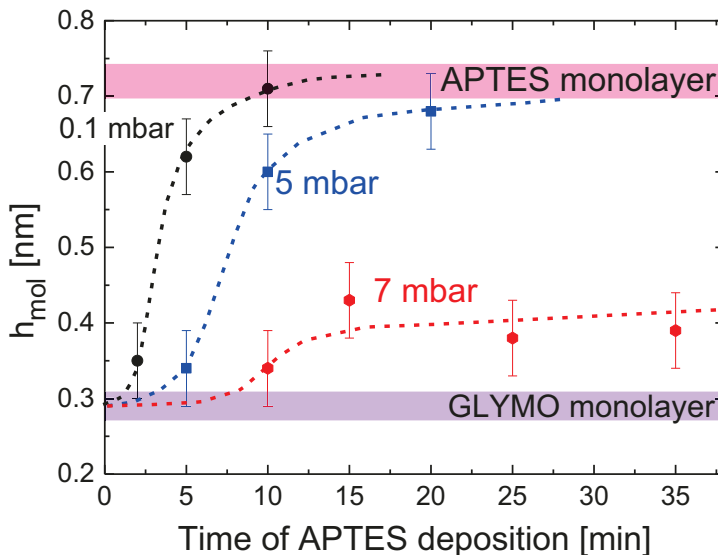


Figure 32. Effective thickness obtained via ellipsometry (see Figure 31) of mixed monolayers of APTES and GLYMO deposited in the same way as shown in Figure 30B, but at different pressures and times for the APTES deposition. Additionally, values for monolayers of APTES and GLYMO are indicated by the pink and purple areas, respectively.

There are a number of interesting features visible in Figure 32:

- (i) Layer growth generally depends on the N_2 pressure during deposition. The lower the N_2 pressure, the higher the vapor pressure of the molecule is. Therefore, the deposition of APTES is faster for lower pressures, which results in a stronger increase in thickness over time for a low N_2 pressure.
- (ii) For N_2 pressures of 5 mbar and 0.1 mbar, the APTES monolayer appears to be completed within less than 35 min. For the large N_2 pressure of 7 mbar, the maximum deposition time of 35 minutes is not sufficient for the formation of a complete APTES layer. Longer deposition times have not been tested. However, it is expected that even for this pressure a complete APTES monolayer could be established.

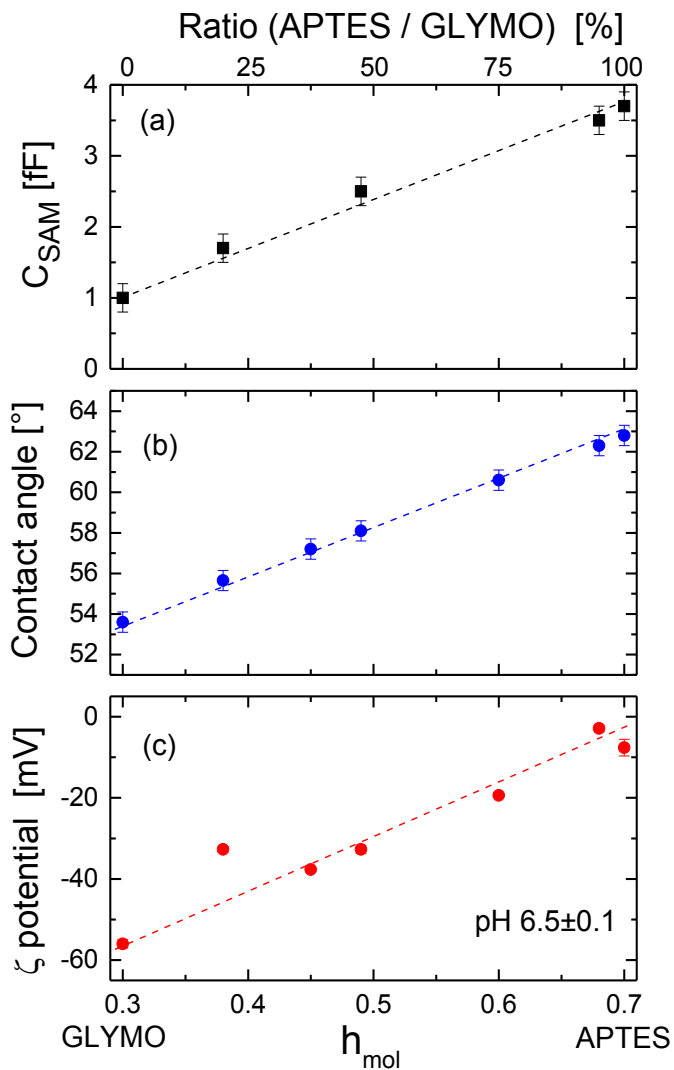


Figure 33. (a) Capacitance, (b) wetting angle, and (c) surface potential (measured in a working electrolyte solution of KCl (1mM) at a pH of 6.5 ± 0.1) of mixed monolayers of APTES and GLYMO as a function of (bottom) the effective thickness of the layer determined via ellipsometry and (top) expected ratio of the molecular components in the layer.

(iii) Furthermore, we see a delayed onset of growth for all pressures, which could indicate a nucleation step of the molecular layer. The delay seems to increase with increasing N_2 pressure, i.e. reduction of the APTES partial pressure and its deposition rate.

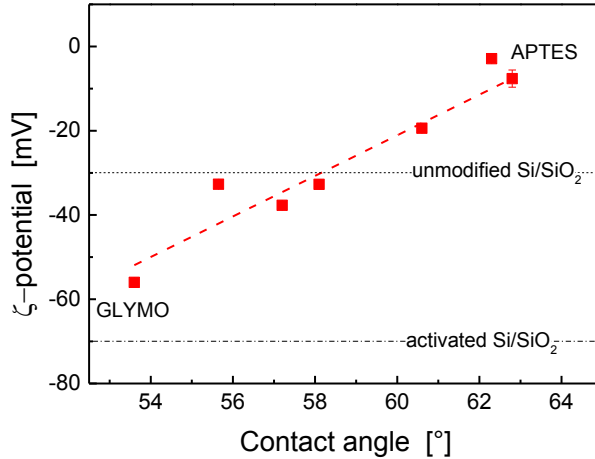


Figure 34. Correlation between ζ -potential (measured in 1mM KCl at a pH of 6.5 ± 0.1) and contact angle of mixed monolayers with different ratios of APTES and GLYMO. The dashed lines refer to the ζ -potential typical of virgin and activated SiO_2 -terminated Si, respectively, which were used as substrates for the measurements.

In concluding this section, we can state that the method of successive deposition of APTES and GLYMO using different times and pressures for the APTES deposition enables the fabrication of mixed layers with various thicknesses in a very controlled manner.

In the following, we analyze some of the properties of the mixed layers. Figure 33 demonstrates the correlation between the ex situ ellipsometry measurements and the molecular contribution to (a) the capacitance C_{SAM} , (b) the contact angle, and (c) the ζ -potential of the layers. The ellipsometry measurements for the different mixed monolayer compositions ranged from $h_{mol} \approx 0.31$ nm for monolayers of pure GLYMO to $h_{mol} \approx 0.73$ nm for pure APTES. All three properties – capacitance C_{mol} , contact angle, and ζ -potential – show a linear correlation with the thickness h_{mol} . The capacitance of the monolayers varies from 1fF to 3.7fF, the contact angle values range from 54° to 63° , and the surface potential measured in a working electrolyte solution of KCl (1 mM) at a pH of 6.5 ± 0.1 changes from ~ -57 mV for pure GLYMO to ~ -10 mV for pure APTES. The perfect linear dependence of all parameters indicates that the correlation between the layer thickness (bottom axis) and composition (top axis) assumed in Figure 33 is justified. This means

that the effective layer thickness is most likely caused by the ratio of APTES and GLYMO molecules in the layer, which also affects the layer properties in a well-defined way.

However, other correlations might also be of interest for applications. For example, surface charge is an important feature of surfaces. Cell membranes, for instance, are negatively charged at physiological pH. Therefore, engineering the surface potential by means of the APTES–GLYMO ratio might improve cell adhesion,^{70,71} cell proliferation, or even gene expression.⁷² The engineering of the surface potential in connection with a “simple” analysis tool might thus be of interest for various biophysical applications.^{70,72,73} In Figure 34, we demonstrate that our method is capable of achieving this. It shows how the surface potential can be (i) engineered via the variation of the APTES–GLYMO ratio and (ii) determined by relatively simple contact angle analysis.

IV.3 Engineering of cortical neurons growth density and enhancing MEA coupling via mixed SAMs

An in-depth understanding of the interface between cells and implantable surfaces is one of the key for coupling electrically excitable cells and bioelectronics devices. Recently, different approaches for tailoring surface properties for enhancing of cell adhesion and various devices with bio-

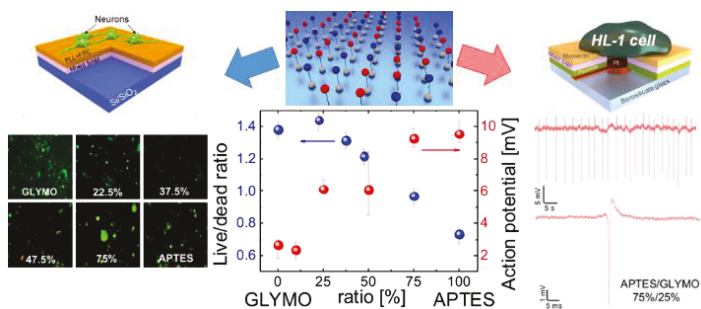


Figure 35. Schematic image of the impact of mixed monolayers on biological applications demonstrated for the control of the growth density and live/dead ratio of neurons and cell-chip communication between HL-1 cells and MEAs.

compatible surfaces have been introduced in order to control the cell growth, stimulate and record electrical signals emanating from inside of the cell. It still remains an open question how to create an ideal surface in a precisely controllable way for cells to couple to various materials.

In this chapter we present a specific engineering of the cell interface with two widely used surfaces Si/SiO₂ and polyimide. While basic methods for cell adhesion were shown for these approaches before, a systematic investigation linking experimental data with both to control the growth density and enhance the action potential signal from cells was not presented so far. Deposited from the vapor phase mixed self-assembled monolayers show a great impact on the neuronal and HL-1 cells growth, action potential signal detection on MEA and reusability of the samples.

IV.2.1 PLL deposition on the mixed molecular SAMs

First, we analyzed the potential of mixed APTES-GLYMO SAMs for biological applications, by depositing poly(L-lysine) (PLL) with fluorescein isothiocyanate marker (FITC) solution onto the mixed molecular layers. The fluorescent marker was added for optical inspection. PLL is a homopolypeptide that belongs to the group of cationic polymers. At pH 7, PLL has positively charged hydrophilic amino groups. The PLL was deposited onto the mixed molecular layers by coating the film with a drop (45 μl) of a PLL+FITC in Gey's Balanced Salt Solution (GBSS) (10 $\mu\text{g}/\text{mL}$) and keeping the sample protected from exposure to light at room temperature for 1 hour. After deposition, the PLL+FITC that was not bound to the molecular layer was removed by rinsing with GBSS.

Due to its amino group the PLL is expected to only bind to the epoxy functional group of GLYMO and not to the amino group of APTES. As a consequence, it is assumed that the amount of PLL+FITC decreases with an increasing amount of APTES in the mixed layer. The intensity of the fluorescence of the PLL layer should therefore decrease with an increasing amount of APTES – i.e. a decreasing amount of GLYMO – in the underlying mixed layer. This correlation is observed (see Figure 36b), indicating that the coverage of the surface with PLL can be controlled by the APTES–GLYMO ratio of the underlying mixed layer.

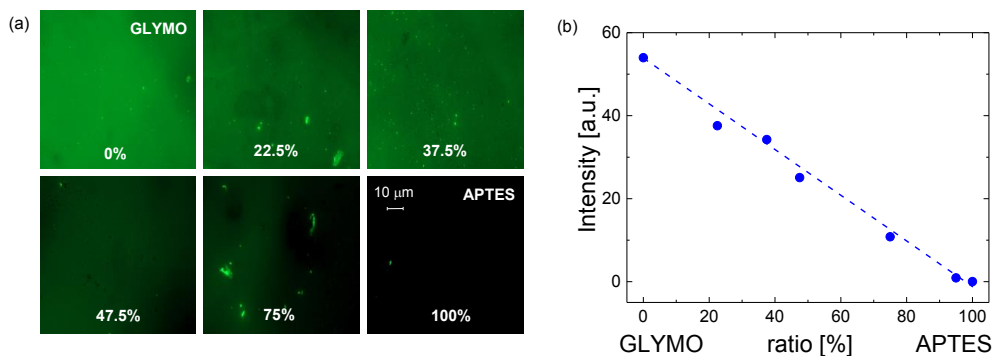


Figure 36. (a) Fluorescence microscope image of samples (SiO_2 terminated Si) with mixed monolayers (the percentage given in the images refers to the fraction of APTES in the layer) coated with PLL+FITC (all with exposure time 600ms) and (b) resulting intensity of PLL+FITC fluorescence as a function of the APTES–GLYMO ratio.

IV.2.2 Neuron growth density on mixed molecular SAMs

After the investigation of the coating dependence of PLL on mixed molecular SAMs, Si/SiO₂ substrates mentioned above were used as culture substrates for primary cortical neurons. For evaluation living cells were fluorescently stained (see chapter III.5.2). Furthermore, we analyze images obtained from different parts of the samples:

- (i) cells inside the PLL coated area (see Figure 38a),
- (ii) cells on the border of the PLL coated area and the Si/SiO₂ area covered only with mixed films (see Figure 39)
- (iii) cells on the Si/SiO₂ area covered only with mixed films (see Figure 40a)

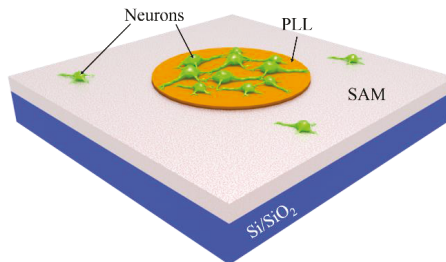


Figure 37. Sketch of SiO₂ terminated Si sample covered with mixed molecular monolayers, PLL coated area and neurons on the surface.

Only where GLYMO is deposited, we expect that PLL can become covalently bonded to the epoxy functional group of GLYMO, so that the GLYMO acts as a linker between the peptide and the Si/SiO₂ surface. After sterilization, remaining GLYMO epoxy groups react during the sterilization process. Neurons adhere to areas of positive charge. Therefore, they should bind only to the amino group of PLL or APTES. In areas where PLL was coated the dominant factor for cell adhesion is expected to be the concentration of PLL (proportional to the concentration of GLYMO), while in uncoated areas the cell adhesion is expected to be dependent on the concentration of APTES. Meaning that on these images we either have cells connected to PLL or to APTES.

Neurons on PLL coated area. Let us first consider the cell growth inside the PLL coated area. On Figure 38 it is clearly shown that cells on PLL tend to grow homogeneously distributed (see Figure 38 b-c) and on APTES they form huge clusters (neurospheres), which are floating above the surface itself. These neurospheres use neurites to fix themselves to a small number of points either directly on the surface or on other cells. Similar to FITC fluorescence in the PLL treated area, the live/dead ratio of neurons decreased with an increasing amount of APTES – i.e. a decreasing amount of GLYMO – in the underlying mixed layer (see Figure 38h). This plot shows that the largest live/dead ratio is not at either end of the concentration scale. There is kind of a “sweet” spot for the molecules at 22.5% of APTES (Figure 38c), however the total amount of both live and dead cells on this sample is smaller than on PLL treated pure GLYMO. This suggests a slightly less adhesive surface overall, where both live but weakly adhered and dead cells may be washed away during medium changes.

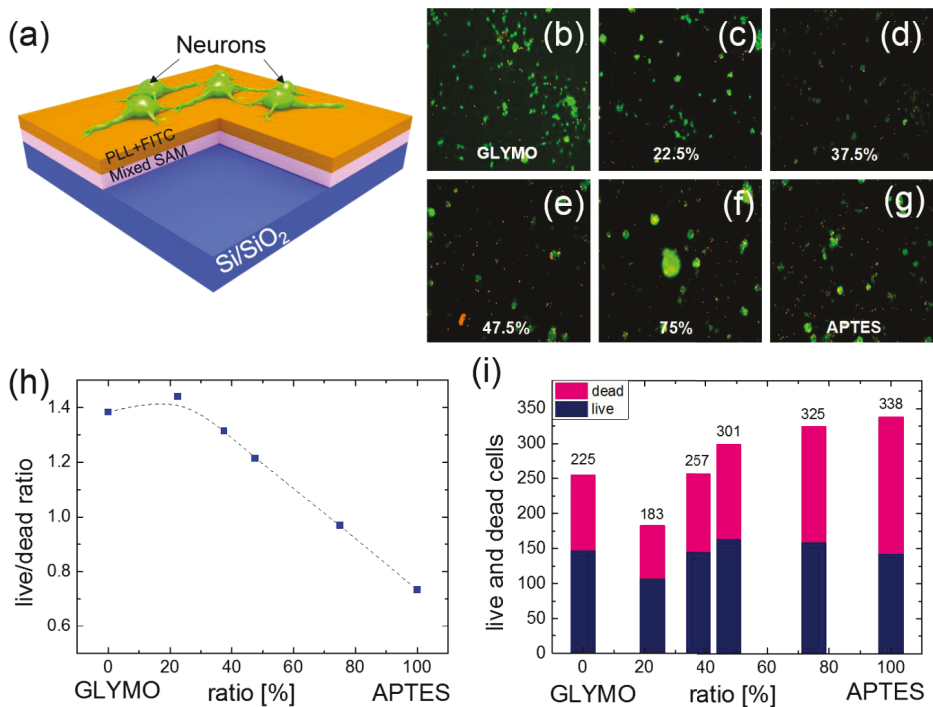


Figure 38. (a) Schematic sketch of the investigated structure. Neurons on PLL+FITC and mixed molecular SAMs. Fluorescence microscope images of Si/SiO₂ substrate with different APTES+GLYMO ratios ranging from pure GLYMO (b) 22.5% (c), 37.5% (d), 47.5% (e), 77.5% (f) APTES and pure APTES (g) coated with PLL+FITC and rat cortical neurons. Live cells are stained with calcien-AM (green), dead cells are marked with ethidium homodimer (orange). (h) shows the live/dead ratio and (i) represents the amount of live and dead rat cortical neurons as function of APTES on the surface of Si/SiO₂ samples coated with PLL+FITC. The total area is 580 $\mu\text{m} \times 580 \mu\text{m}$ (0.3364 mm²)

Overall, Figure 38h demonstrates that samples with higher amount of PLL bound to GLYMO are preferable for neurons with respect to the live/dead ratio (Figure 38b-e). Figure 38i shows that amount of live cells on different samples is relatively similar at about 410 \pm 30 mm⁻², except maybe for the sample with 22.5% of APTES, whereas the amount of dead cells increases with increasing amount of APTES.

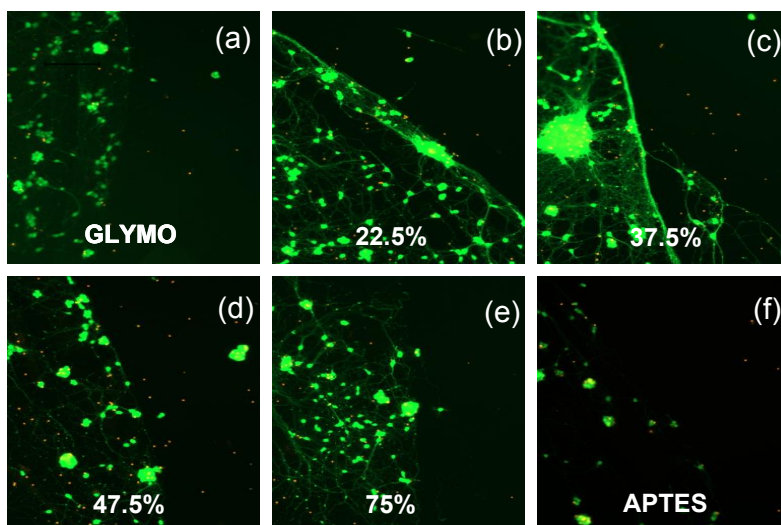


Figure 39. Fluorescence microscope image taken at the border of PLL+FITC treated area and cultured with rat cortical neurons for molecular SAMs with pure GLYMO (a), 22.5% (b), 37.5% (c), 47.5% (d), 77.5% (e) APTES and pure APTES (f). Live cells are marked with calcein-AM (green), dead cells are marked with ethidium homodimer (orange).

Neurons at the border of PLL coated area. Figure 39 shows images of neurons on the border of the PLL treated area on various mixed SAMs. This figure shows that cells prefer to stay inside of the PLL ring and most do not grow outside of that area directly on the mixed monolayers. However, there is a noticeable feature, which is shown on Figure 39b-c. On the samples with 22.5% and 37.5% APTES neurites distinctly follow the border and form bundles. The reason for such behavior should still be investigated further. We can see few possible explanations for that, either this is a resulting influence of different charges, created by unoccupied neutral functional epoxy group of GLYMO and positively charged amino functional group of APTES. Or at these ratios difference in docking sites for PLL and as a result for cells is extremely large, therefore, cells at any cost prefer to stay inside the PLL drop. Most likely, both of these explanations (i.e., different charges and different amount of docking sites) are responsible for those neuronal bundles. This behavior might be considered for guided neuronal growth in bioelectronics applications.

Neurons on the mixed molecular SAM. Next, we consider the amount of cells growing outside the region treated by PLL on various GLYMO/APTES ratios (see Figure 40a). Meaning that the Si/SiO₂ sample is covered only by mixed molecular SAMs in this region. On the SAMs viable cell growth can only be observed on samples with 75% and 100% of APTES (see Figure 40f-g). Due

to neurons' attachment to the amino functional group of APTES and not to epoxy functional group of GLYMO, this dependence is understandable. This is also clearly seen on the sample with a pure GLYMO layer where cells do not attached to the surface at all, because there are no docking sites for the cell adhesion. Live/dead ratio of cells on those surfaces (see Figure 40h) is inverse to those areas treated with the PLL (Figure 38h).

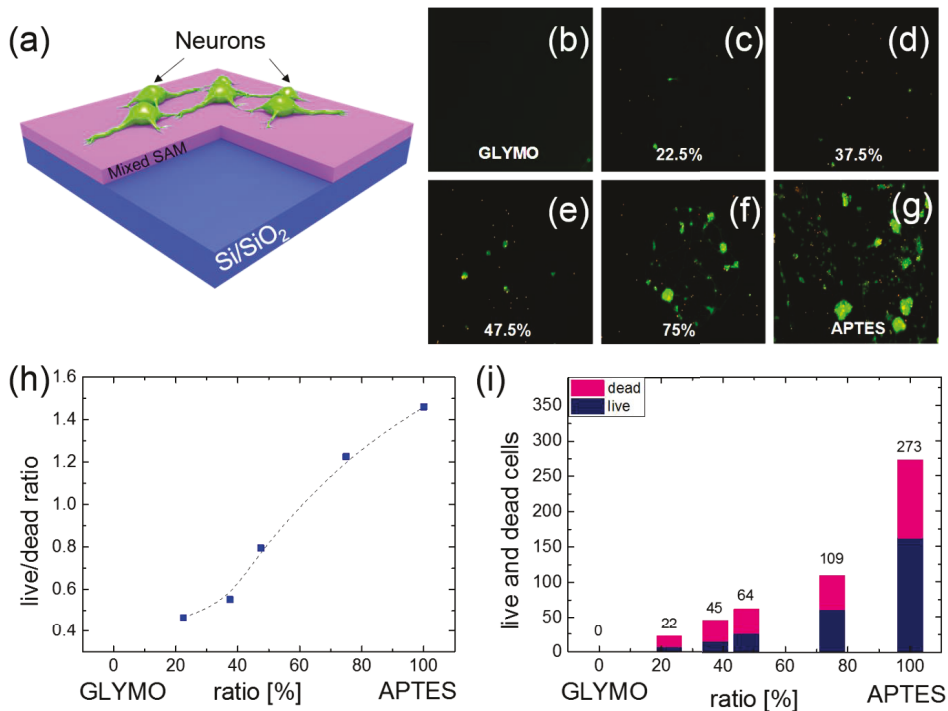


Figure 40. (a) Schematic sketch of the investigated structure. Fluorescence microscope images of Si/SiO₂ substrate with different APTES+GLYMO ratios ranging from pure GLYMO (b) 22.5% (c), 37.5% (d), 47.5% (e), 77.5% (f) APTES and pure APTES (g) coated with rat cortical neurons. Live cells are marked with calcein-AM (green), dead cells are marked with ethidium homodimer (orange). (h) and (i) show the live/dead ratio as amount of live and dead rat cortical neurons as function of APTES percent on the surface of Si/SiO₂ samples, respectively.

Without PLL, all samples where there is more GLYMO than APTES (see Figure 40b-e) show live/dead ratio less than 1. Samples with more APTES molecules (see Figure 40f-g) show live/dead ratio higher than 1. The total amount of cells increases with an increase of APTES ratio in the mixed films (see Figure 40i), suggesting non-specific binding to the charged surface is the dominant phenomenon.

To summarize this part we can claim further:

- (i) cells prefer to grow on surfaces covered by PLL rather than on APTES, although they both have amino groups for neuronal adhesion,
- (ii) using mixed films we can influence different cell growth parameters like:
 - live/dead ratio,
 - homogeneity of cell distribution on the surface,
 - total amount of cells on the surface,
 - distance between cells and substrate, and
 - restriction of cell growth to specific areas
- (iii) at a certain APTES/GLYMO ratios (here 22.5% and 37.5% APTES) cells tend to create thick neurite bundles on the border between PLL covered and uncovered areas, which can be of interest for bioelectronics applications.

IV.2.3 Cell-chip communication

In order to provide a comprehensive statistical analysis of mixed monolayers influence on extensive cellular recordings, we used in-house fabricated 64 channel amplifier system. MEAs are fabricated on a borosilicate wafer with 10 nm of Cr as an adhesive sublayer, electrodes are made of 200 nm of Pt and covered with 3 μ m of polyimide HD8820, with 64 24 μ m diameter openings down to the Pt with as the electrodes. The MEAs then were covered by mixed APTES/GLYMO monolayers using the same parameters as for the Si/SiO₂ samples.⁶³ In order to show the applicability of the devices for bioelectronics applications, the devices were encapsulated and prepared for cell culture (see chapter III.5.3). Cardiomyocyte-like cells (HL-1 cell line)⁷⁴ are further cultured on the chips' surface (see Figure 41e). The cell potential changes were later measured at on a custom built amplifier system, BioMAS, against a silver/silver chloride reference electrode placed directly in the cell culture medium.

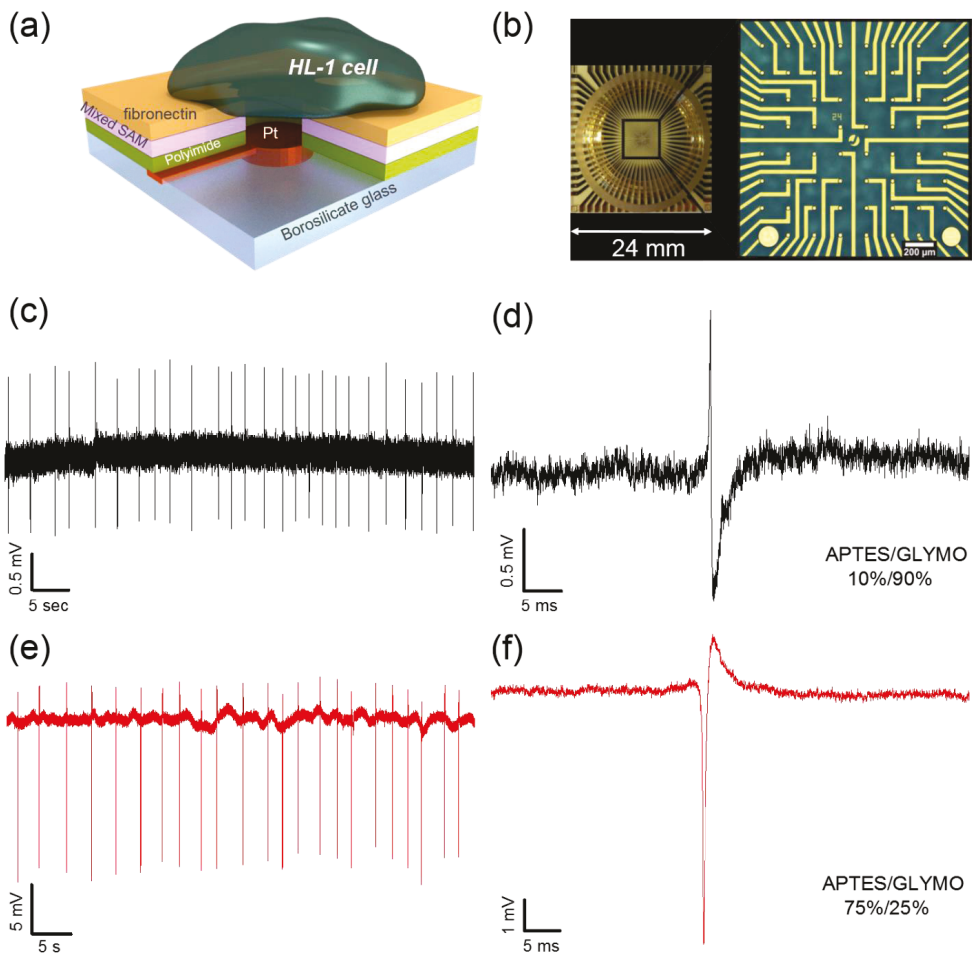


Figure 41. Schematic sketch of the investigated MEA structure (a). Image of the MEA structure and electrode array (b). Action potential of HL-1 cells on MEAs coated by APTES/GLYMO mixed monolayers and fibronectin (e-f). (e).

A typical time trace recording from a MEAs covered by mixed films with HL-1 action potentials is shown in Figure 41c and e, for samples with 10% and 75% APTES, respectively. The cells are beating (producing repetitive action potential (AP) that propagate through the whole cellular layer, accompanied by cell contraction to visually confirm cell activity) with a rate about 23 bpm and an amplitude of 2.8 ± 0.2 mV for lowest obtained signal (see Figure 41d) and 9.4 ± 0.6 mV for highest obtained signal (see Figure 41f). This is the case for the best coupling per recording and chips with similar electrode arrays. Considering the noise level of $200 \mu\text{V}$, the overall signal-to-noise ratio

(SNR) is 14 ± 1 (see Figure 41d), which is considerably better than reported previously^{75,76}. The shape of the APs is shown in Figure 41d and f. The shape of the action potential, in agreement with previous works, represents a very good sealing between the cell and the electronic device^{77,78}. However, overall results of action potential measurement exceeded our expectation. Signals obtained from samples with 75% and 100% of APTES show at least an order of magnitude higher signals than previously observed from protein coated MEAs with planar electrodes. Even samples with the lowest amplitude of signal show AP values at least 2 mV (see Figure 42).

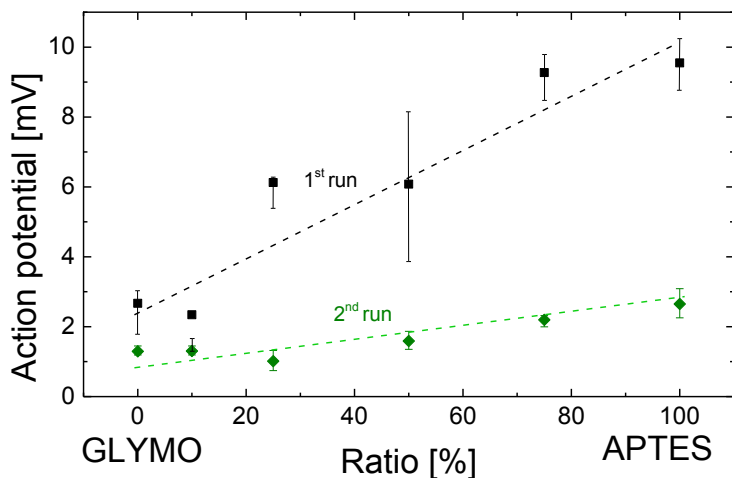


Figure 42. Action potential as a function of molecular ratio of APTES/GLYMO mixed monolayers for the 1st (black) and 2nd (green) cell culturing on one and the same MEA. For the second culturing only the cells were removed.

The AP signal dependence on APTES/GLYMO ratio represent a particular interest. Initially it was expected that the behavior will be similar to the neuronal dependence on the Si/SiO₂ samples, where more GLYMO resulted in more cells attached to the surface. Here we have fibronectin instead of PLL as a protein linker between the surface and the HL-1 cells. In contrast to neurons, HL-1 cells attach and spread on APTES molecules without forming semi-detached cell clusters as the neurons did. Therefore, HL-1 behaved similarly on fibronectin and APTES layers. According to previous works the thickness of the fibronectin layer is about 8.7nm⁷⁹. Thus, this distance from the metal electrode to the cell is larger when fibronectin is present than for the mixed film alone. This increased distance can increase the electrical leak current between the cell and the device during the action potential measurement. This could explain the probability of decreased signal level obtained from samples with higher GLYMO ratio (higher fibronectin ratio as a result). Another explanation could be that the mixed molecular SAM protects the electronic from

activation and coating with fibronectin. This would lead to an improved coupling of the cells' electronic signal to the electrode. The exact explanation needs more research.

In order to demonstrate the ability to reuse samples with mixed films, all MEAs were cleaned in the surfactant 2% Helmanex III in ultrasound followed by 5 min in bidest water in ultrasound. During the cleaning the HL-1 cell culture was removed from the samples, however, the mixed films and the covalently bound protein remained. After cleaning, the devices were re-sterilized prior to cell culture in 70% ethanol (see chapter III.5.3). Next, a new round of HL-1 cells was cultured on the surface. The devices were measured according to the previous experiments.

The typical time trace recording from a reused MEAs covered by mixed films with HL-1 action potentials were similar to those measured in the first run. The tendency of increasing AP values from GLYMO to APTES samples is still present (see Figure 42). However, the amplitude of AP peaks became considerably smaller. The smallest average signal is 0.8mV for sample with 25% of APTES and the highest average signal is 2.6mV, which is still comparable or even better than previously reported^{75,76}. This reproducibility of results is applicable for all experiments in this chapter, i.e. neuronal cultures on Si/SiO₂ and HL-1 cells on MEAs in the end show reproducible results with just overall smaller amount of cells attached to the surface (neurons on Si/SiO₂), or lower amplitude for AP (for HL-1 cells on MEAs). That strengthens the significance of this work, because mixed films bring not only possibilities of tailoring surface properties in terms of controlling the growth of cell cultures on the surface or enhancing AP values measured from these cells, but the ability to use a device over again with minimal re-processing, thereby increasing productivity and reducing costs of experiments. This is particularly relevant for substrates with patterned adhesive regions, since patterning methods such as microcontact printing, optical lithography, and laser-writing are all very time (and money) consuming.

Summary

Optimization of the interface between bio objects (e.g. cells) and non-organic surfaces (silicon chips, substrates or inorganic electronic) is one of the major keys to the future of bioengineering. It allows to improve the cell adhesion to rigid or flexible substrates, control the immobilization of neurons or guidance of neurite outgrowths on the surface of an electronic sensors, create stable protein patterned arrays, might enhance the cell-chip communication, and improve the organ-device interface for biomedical devices such as prosthetics or implants. These goals heavily depend on the physical and chemical properties of the interface, in-depth understanding of which gives the possibility for the proper interface modification in the direction of biocompatibility and improvement of bioelectronics.

In this dissertation, we first demonstrate a novel in situ and extremely sensitive detection method for the analysis of the electronic properties of molecular layers and the control of the molecular layer deposition of self-assembled monolayers of one or more types of molecules. The MLD setup allows:

- (i) to perform all process steps including surface activation, deposition of different molecules (single monolayers and mixed molecular monolayers) from the gas phase and subsequent removal of superfluous molecules without braking the vacuum, and
- (ii) to control the deposition and record the dielectric permittivity, dielectric losses, and conductivity of the molecular layers throughout the entire deposition process using a capacitive sensor based on planar interdigitated electrodes.

The resulting permittivity of the SAM (electric field in the plane of the layer) turns out to be much larger (4–9 times) than the permittivity of the molecules in the liquid state. This discrepancy can be explained by the anisotropy of the permittivity of the molecule, the difference in the molecular density in SAMs and liquids, or a combination of both explanations. The permittivity of the SAM might be an indication of the quality (density, order, and orientation) of the SAM. Values of $\epsilon_{\text{SAM}} \approx 51$ obtained for our SAMs of APTES demonstrate that molecular layers have a high potential for a number of electronic applications that require high permittivity.

Second, with the help of the in situ capacitive characterization we achieved a precise control of the ratio of two molecules APTES and GLYMO with different functional groups using different times and pressures for the APTES deposition. The resulting mixed APTES–GLYMO monolayers exhibit a perfect linear correlation between the effective thickness, capacitive contribution, wetting angle, and surface potential on the APTES–GLYMO ratio.

Third, we can not only improve the substrate's biocompatibility via these SAMs but even affect the neuronal growth density and live/dead ratio control on Si/SiO₂ substrates coated with mixed molecular monolayers with and without PLL.

Finally, we demonstrate a strongly improved cell-chip coupling and obtained high signals (up to 9.4 ± 0.6 mV) for the action potential of HL-1 cells on MEAs covered with the mixed molecular layers.

Although only a limiting number of model systems was discussed, this work demonstrates the great potential of studying different methods of controlled interface modification. It brings promising perspectives for the construction of reliable and productive devices for biological applications like biosensors, for purely biological problems like adhesion and guiding of proteins or cells on inorganic or organic surfaces. Moreover, the developed method of tailoring the interface properties gives an ability to use a device over again with minimal re-processing, thereby increasing productivity and reducing costs of experiments.

This study suggests that tailoring of the interface properties via the novel MLD technology used in this work with in situ deposition control seems to be very powerful and is a crucial consideration for the development of new materials and devices for bioelectrical and even biological applications ranging from medical implants to biosensors.

References

- (1) Sveshnikova, G. V.; Kol'tsov, S. I.; Aleskovskii, V. B. No Title. *J. Appl. Chem. USSR* **1970**, *43*, 432–434.
- (2) Aleskovskii, V. B. No Title. *J. Appl. Chem. USSR* **1974**, *47*, 2145–2157.
- (3) Suntola, T.; Antson, J. Method for Producing Compound Thin Films.
- (4) Puurunen, R. L. Surface Chemistry of Atomic Layer Deposition: A Case Study for the Trimethylaluminum/water Process. *J. Appl. Phys.* **2005**, *97* (12), 121301.
- (5) Yoshimura, T.; Tatsuura, S.; Sotoyama, W. Polymer Films Formed with Monolayer Growth Steps by Molecular Layer Deposition. *Appl. Phys. Lett.* **1991**, *59* (4), 482–484.
- (6) Kubono, A.; Yuasa, N.; Shao, H.-L.; Umemoto, S.; Okui, N. In-Situ Study on Alternating Vapor Deposition Polymerization of Alkyl Polyamide with Normal Molecular Orientation. *Thin Solid Films* **1996**, *289* (1-2), 107–111.
- (7) Nagai, A.; Shao, H.; Umemoto, S.; Kikutani, T.; Okui, N. Quadruple Aliphatic Polyamide Systems Prepared by a Layer-by-Layer Alternating Vapour Deposition Method. *High Perform. Polym.* **2001**, *13* (2), S169–S179.
- (8) Shao, H.-I.; Umemoto, S.; Kikutani, T.; Okui, N. Layer-by-Layer Polycondensation of Nylon 66 by Alternating Vapour Deposition Polymerization. *Polymer (Guildf)*. **1997**, *38* (2), 459–462.
- (9) Yoshimura, T.; Tatsuura, S.; Sotoyama, W.; Matsuura, A.; Hayano, T. Quantum Wire and Dot Formation by Chemical Vapor Deposition and Molecular Layer Deposition of One-dimensional Conjugated Polymer. *Appl. Phys. Lett.* **1992**, *60* (3), 268–270.
- (10) Lee, B. H.; Ryu, M. K.; Choi, S.-Y.; Lee, K.-H.; Im, S.; Sung, M. M. Rapid Vapor-Phase Fabrication of Organic–Inorganic Hybrid Superlattices with Monolayer Precision. *J. Am. Chem. Soc.* **2007**, *129* (51), 16034–16041.
- (11) Smirnov, V. M.; Zemtsova, E. G.; Belikov, A. A.; Zheldakov, I. L.; Morozov, P. E.; Polyachonok, O. G.; Aleskovskii, V. B. Chemical Design of Quasi-One-Dimensional Organoiron Nanostructures Fixed on an Inorganic Matrix and Study of Their Magnetic Properties. *Dokl. Phys. Chem.* **2007**, *413* (2), 95–98.
- (12) Dameron, A. A.; Seghete, D.; Burton, B. B.; Davidson, S. D.; Cavanagh, A. S.; Bertrand, J. A.; George, S. M. Molecular Layer Deposition of Alucone Polymer Films Using Trimethylaluminum and Ethylene Glycol. *Chem. Mater.* **2008**, *20* (10), 3315–3326.
- (13) Nilsen, O.; Klepper, K.; Nielsen, H.; Fjellvåg, H. Deposition of Organic- Inorganic Hybrid Materials by Atomic Layer Deposition. In *ECS Transactions*; ECS, 2008; Vol. 16, pp 3–14.
- (14) Sood, A.; Sundberg, P.; Malm, J.; Karppinen, M. Layer-by-Layer Deposition of Ti–4,4'-Oxydianiline Hybrid Thin Films. *Appl. Surf. Sci.* **2011**, *257* (15), 6435–6439.
- (15) Liang, X.; Yu, M.; Li, J.; Jiang, Y.-B.; Weimer, A. W. Ultra-Thin Microporous–mesoporous Metal Oxide Films Prepared by Molecular Layer Deposition (MLD). *Chem. Commun.* **2009**, No. 46, 7140.
- (16) Seghete, D.; Davidson, B. D.; Hall, R. A.; Chang, Y. J.; Bright, V. M.; George, S. M. Sacrificial Layers

- for Air Gaps in NEMS Using Alucone Molecular Layer Deposition. *Sensors Actuators A Phys.* **2009**, *155* (1), 8–15.
- (17) Gabriel, N. T.; Talghader, J. J. Thermal Conductivity and Refractive Index of Hafnia-Alumina Nanolaminates. *J. Appl. Phys.* **2011**, *110* (4), 043526.
 - (18) Smith, S. W.; McAuliffe, K. G.; Conley, J. F. Atomic Layer Deposited High-K Nanolaminate Capacitors. *Solid. State. Electron.* **2010**, *54* (10), 1076–1082.
 - (19) Heo, J.; Liu, Y.; Sinersuksakul, P.; Li, Z.; Sun, L.; Noh, W.; Gordon, R. G. (Sn,Al)O_x Films Grown by Atomic Layer Deposition. *J. Phys. Chem. C* **2011**, *115* (20), 10277–10283.
 - (20) Elam, J. W.; Sechrist, Z. A.; George, S. M. ZnO/Al₂O₃ Nanolaminates Fabricated by Atomic Layer Deposition: Growth and Surface Roughness Measurements. *Thin Solid Films* **2002**, *414* (1), 43–55.
 - (21) George, S. M. Atomic Layer Deposition: An Overview. *Chem. Rev.* **2010**, *110* (1), 111–131.
 - (22) Miikkulainen, V.; Leskelä, M.; Ritala, M.; Puurunen, R. L. Crystallinity of Inorganic Films Grown by Atomic Layer Deposition: Overview and General Trends. *J. Appl. Phys.* **2013**, *113* (2), 021301.
 - (23) Knez, M.; Nielsch, K.; Niinistö, L. Synthesis and Surface Engineering of Complex Nanostructures by Atomic Layer Deposition. *Adv. Mater.* **2007**, *19* (21), 3425–3438.
 - (24) Leskelä, M.; Ritala, M.; Nilsen, O. Novel Materials by Atomic Layer Deposition and Molecular Layer Deposition. *MRS Bull.* **2011**, *36* (11), 877–884.
 - (25) George, S. M. *The Strem Chemiker*; 2011.
 - (26) George, S. M.; Yoon, B.; Dameron, A. A. Surface Chemistry for Molecular Layer Deposition of Organic and Hybrid Organic–Inorganic Polymers. *Acc. Chem. Res.* **2009**, *42* (4), 498–508.
 - (27) Lee, B. H.; Yoon, B.; Abdulgatov, A. I.; Hall, R. A.; George, S. M. Growth and Properties of Hybrid Organic–Inorganic Metalcone Films Using Molecular Layer Deposition Techniques. *Adv. Funct. Mater.* **2013**, *23* (5), 532–546.
 - (28) Yoshimura, T.; Yoshino, C.; Sasaki, K.; Sato, T.; Seki, M. Cancer Therapy Utilizing Molecular Layer Deposition and Self-Organized Lightwave Network: Proposal and Theoretical Prediction. *IEEE J. Sel. Top. Quantum Electron.* **2012**, *18* (3), 1192–1199.
 - (29) King, D. M.; Liang, X.; Weimer, A. W. Functionalization of Fine Particles Using Atomic and Molecular Layer Deposition. In *ECS Transactions*; ECS, 2009; pp 163–190.
 - (30) Zhou, H.; Bent, S. F. Fabrication of Organic Interfacial Layers by Molecular Layer Deposition: Present Status and Future Opportunities. *J. Vac. Sci. Technol. A Vacuum, Surfaces, Film.* **2013**, *31* (4), 040801.
 - (31) Sundberg, P.; Karppinen, M. Organic and Inorganic–Organic Thin Film Structures by Molecular Layer Deposition: A Review. *Beilstein J. Nanotechnol.* **2014**, *5* (1), 1104–1136.
 - (32) Gilles, S. Chemical Modification of Silicon Surfaces for the Application in Soft Lithography. **2007**.
 - (33) Greben, K. Modification and Characterization of Potential Bioelectronic Interfaces. **2015**, *101*, 76.
 - (34) Kamisetty, N. K.; Pack, S. P.; Nonogawa, M.; Devarayapalli, K. C.; Kodaki, T.; Makino, K. Development of an Efficient Amine-Functionalized Glass Platform by Additional Silanization

- Treatment with Alkylsilane. *Anal. Bioanal. Chem.* **2006**, *386* (6), 1649–1655.
- (35) Sun, Y.; Wang, H.; Sun, C. Amperometric Glucose Biosensor Based on Layer-by-Layer Covalent Attachment of AMWNTs and IO(4)(-)-Oxidized GOx. *Biosens. Bioelectron.* **2008**, *24* (1), 22–28.
- (36) Tessier, D. C.; Boughaba, S.; Arbour, M.; Roos, P.; Pan, G. Improved Surface Sensing of DNA on Gas-Etched Porous Silicon. *Sensors Actuators, B Chem.* **2006**, *120* (1), 220–230.
- (37) Sterzynska, K.; Budna, J.; Frydrych-Tomczak, E.; Hreczycho, G.; Malinska, A.; Maciejewski, H.; Zabel, M. Silane-Modified Surfaces in Specific Antibody-Mediated Cell Recognition. *Folia Histochem. Cytobiol.* **2014**, *52* (3), 250–255.
- (38) Louis, C.; Bazzi, R.; Marquette, C. A.; Bridot, J. L.; Roux, S.; Ledoux, G.; Mercier, B.; Blum, L.; Perriat, P.; Tillement, O. Nanosized Hybrid Particles with Double Luminescence for Biological Labeling. *Chem. Mater.* **2005**, *17* (7), 1673–1682.
- (39) Enders, D.; Nagao, T.; Pucci, A.; Nakayama, T. Reversible Adsorption of Au Nanoparticles on SiO₂/Si: An in Situ ATR-IR Study. *Surf. Sci.* **2006**, *600* (6), 71–75.
- (40) Kumeria, T.; Santos, A.; Losic, D. Ultrasensitive Nanoporous Interferometric Sensors for Label-Free Detection of Gold (III) Ions. *ACS Appl. Mater. Interfaces* **2013**, *5* (11), 11783–11790.
- (41) Vinoba, M.; Lim, K. S.; Lee, S. K.; Jeong, S. K.; Alagar, M. Immobilization of Human Carbonic Anhydrase on Gold Nanoparticles Assembled onto Amine/thiol-Functionalized Mesoporous SBA-15 for Biomimetic Sequestration of CO₂. *Langmuir* **2011**, *27* (10), 6227–6234.
- (42) Shao, L.; Jeon, J. W.; Lutkenhaus, J. L. Polyaniline/vanadium Pentoxide Layer-by-Layer Electrodes for Energy Storage. *Chem. Mater.* **2012**, *24* (1), 181–189.
- (43) Balasundaram, G.; Sato, M.; Webster, T. J. Using Hydroxyapatite Nanoparticles and Decreased Crystallinity to Promote Osteoblast Adhesion Similar to Functionalizing with RGD. *Biomaterials* **2006**, *27* (14), 2798–2805.
- (44) Sapsford, K. E.; Ligler, F. S. Real-Time Analysis of Protein Adsorption to a Variety of Thin Films. *Biosens. Bioelectron.* **2004**, *19* (9), 1045–1055.
- (45) Kuddannaya, S.; Chuah, Y. Surface Chemical Modification of Poly (dimethylsiloxane) for the Enhanced Adhesion and Proliferation of Mesenchymal Stem Cells. *ACS Appl. Mater. Interfaces* **2013**, *5*, 9777–9784.
- (46) Sun, W.; Wang, L.; Wu, T.; Wang, M.; Yang, Z.; Pan, Y.; Liu, G. Inhibiting the Corrosion-Promotion Activity of Graphene. *Chem. Mater.* **2015**, *27* (7), 2367–2373.
- (47) Vandenberg, E. T.; Bertilsson, L.; Liedberg, B.; Uvdal, K.; Erlandsson, R.; Elwing, H.; Lundström, I. Structure of 3-Aminopropyl Triethoxy Silane on Silicon Oxide. *J. Colloid Interface Sci.* **1991**, *147* (1), 103–118.
- (48) Huang, X.; Huang, H.; Wu, N.; Hu, R.; Zhu, T.; Liu, Z. Investigation of Structure and Chemical States of Self-Assembled Au Nanoscale Particles by Angle-Resolved X-Ray Photoelectron Spectroscopy. *Surf. Sci.* **2000**, *459* (1), 183–190.
- (49) Zhang, F.; Sautter, K.; Larsen, A. M.; Findley, D. A.; Davis, R. C.; Samha, H.; Linford, M. R. Chemical Vapor Deposition of Three Aminosilanes on Silicon Dioxide: Surface Characterization, Stability, Effects of Silane Concentration, and Cyanine Dye Adsorption. *Langmuir* **2010**, *26* (18), 14648–

14654.

- (50) Smith, E. A.; Chen, W. How to Prevent the Loss of Surface Functionality Derived from Aminosilanes. *Langmuir* **2009**, *24* (21), 12405–12409.
- (51) Love, J. C.; Estroff, L. A.; Kriebel, J. K.; Nuzzo, R. G.; Whitesides, G. M. *Self-Assembled Monolayers of Thiolates on Metals as a Form of Nanotechnology*; 2005; Vol. 105.
- (52) Zhuang, Y. X.; Hansen, O.; Knieling, T.; Wang, C.; Rombach, P.; Lang, W.; Benecke, W.; Kehlenbeck, M.; Koblitz, J. Vapor-Phase Self-Assembled Monolayers for Anti-Stiction Applications in MEMS. *J. Microelectromechanical Syst.* **2007**, *16* (6), 1451–1460.
- (53) Gross, R.; Marx, A. *Festkörperphysik*; De Gruyter: Berlin, 1999.
- (54) Lessel, M.; Bäumchen, O.; Klos, M.; Hähl, H.; Fetzer, R.; Seemann, R.; Jacobs, K. Self-Assembled Silane Monolayers: A Step-by-Step High Speed Recipe for High-Quality, Low Energy Surfaces. *Surf. Interface Anal.* **2012**, No. September 2015, 29–31.
- (55) Batyrev, I. G.; Tuttle, B.; Fleetwood, D. M.; Schrimpf, R. D.; Tsetseris, L.; Pantelides, S. T. Reactions of Water Molecules in Silica-Based Network Glasses. *Phys. Rev. Lett.* **2008**, *100* (10), 2–5.
- (56) Greben, K.; Li, P.; Mayer, D.; Offenhäusser, A.; Wördenweber, R. Immobilization and Surface Functionalization of Gold Nanoparticles Monitored via Streaming Current/potential Measurements. *J. Phys. Chem. B* **2015**, *119* (19), 5988–5994.
- (57) Markov, A.; Greben, K.; Mayer, D.; Offenhäusser, A.; Wördenweber, R. In Situ Analysis of the Growth and Dielectric Properties of Organic Self-Assembled Monolayers: A Way to Tailor Organic Layers for Electronic Applications. *ACS Appl. Mater. Interfaces* **2016**, *8* (25), 16451–16456.
- (58) Vendik, O. G.; Nikol'skii, M. A. Simulation of a Multilayer Planar Capacitor. *Tech. Phys.* **2001**, *46* (1), 112–116.
- (59) Vendik, O. G.; Zubko, S. P.; Nikol'skii, M. A. Modeling and Calculation of the Capacitance of a Planar Capacitor Containing a Ferroelectric Thin Film. *Tech. Phys.* **1999**, *44* (4), 349–355.
- (60) Chen, E. C. E.; Chou, S. Y. Characteristics of Coplanar Transmission Lines on Multilayer\substrates: Modeling and Experiments. *IEEE Trans. Microw. Theory Tech.* **1997**, *45* (6), 939–945.
- (61) Broers, A. N.; Hoole Andrew C.F, A. C. F.; Ryan, J. M. Electron Beam Lithography - Resolution Limits. *Microelectron. Eng.* **1996**, *32* (1-4 SPEC. ISS.), 131–142.
- (62) Cai, B. Manipulating the Structural and Electronic Properties of Epitaxial NaNbO_3 . **2016**.
- (63) Markov, A.; Wolf, N.; Yuan, X.; Mayer, D.; Maybeck, V.; Offenhäusser, A.; Wördenweber, R. Controlled Engineering of Oxide Surfaces for Bioelectronics Applications Using Organic Mixed Monolayers. *ACS Appl. Mater. Interfaces* **2017**, *9* (34), 29265–29272.
- (64) Hunter, R. J. *Zeta Potential in Colloid Science: Principles and Applications*; Academic Press: London, 1981.
- (65) Fiorilli, S.; Rivolo, P.; Descrovi, E.; Ricciardi, C.; Pasquardini, L.; Lunelli, L.; Vanzetti, L.; Pederzoli, C.; Onida, B.; Garrone, E. Vapor-Phase Self-Assembled Monolayers of Aminosilane on Plasma-

- Activated Silicon Substrates. *J. Colloid Interface Sci.* **2008**, *321* (1), 235–241.
- (66) Arroyo-Hernandez, M.; Manso-Silvan, M.; Lopez-Elvira, E.; Munoz, A.; Climent, A.; Duart, J. M. M. One Step Processing of Aminofunctionalized Gate Oxides. *Biosens. Bioelectron.* **2007**, *22* (12), 2786–2789.
- (67) Dąbrowski, R.; Kula, P.; Herman, J. High Birefringence Liquid Crystals. *Crystals* **2013**, *3* (3), 443–482.
- (68) Xiang, S.; Xing, G.; Xue, W.; Lu, C.; Lin, J.-M. Comparison of Two Different Deposition Methods of 3-Aminopropyltriethoxysilane on Glass Slides and Their Application in the ThinPrep Cytologic Test. *Analyst* **2012**, *137* (7), 1669–1673.
- (69) Romaner, L.; Heimel, G.; Ambrosch-Draxl, C.; Zojer, E. The Dielectric Constant of Self-Assembled Monolayers. *Adv. Funct. Mater.* **2008**, *18* (24), 3999–4006.
- (70) Xu, L.-P.; Meng, J.; Zhang, S.; Ma, X.; Wang, S. Amplified Effect of Surface Charge on Cell Adhesion by Nanostructures. *Nanoscale* **2016**, No. 0, 1–4.
- (71) Li, P.; Greben, K.; Wördenweber, R.; Simon, U.; Offenhäusser, A.; Mayer, D. Tuning Neuron Adhesion and Neurite Guiding Using Functionalized AuNPs and Backfill Chemistry. *RSC Adv.* **2015**, *5* (49), 39252–39262.
- (72) Hao, L.; Fu, X.; Li, T.; Zhao, N.; Shi, X.; Cui, F.; Du, C.; Wang, Y. Surface Chemistry from Wettability and Charge for the Control of Mesenchymal Stem Cell Fate through Self-Assembled Monolayers. *Colloids Surfaces B Biointerfaces* **2016**, *148*, 549–556.
- (73) Guo, S.; Zhu, X.; Li, M.; Shi, L.; Ong, J. L. T.; Jaczewski, D.; Neoh, K. G. Parallel Control over Surface Charge and Wettability Using Polyelectrolyte Architecture: Effect on Protein Adsorption and Cell Adhesion. *ACS Appl. Mater. Interfaces* **2016**, *8* (44), 30552–30563.
- (74) Claycomb, W. C.; Lanson, N. A.; Stallworth, B. S.; Egeland, D. B.; Delcarpio, J. B.; Bahinski, A.; Izzo, N. J. HL-1 Cells: A Cardiac Muscle Cell Line That Contracts and Retains Phenotypic Characteristics of the Adult Cardiomyocyte. *Proc. Natl. Acad. Sci. U. S. A.* **1998**, *95* (6), 2979–2984.
- (75) Eschermann, J. F.; Stockmann, R.; Hueske, M.; Vu, X. T.; Ingebrandt, S.; Offenhäusser, A. Action Potentials of HL-1 Cells Recorded with Silicon Nanowire Transistors. *Appl. Phys. Lett.* **2009**, *95* (8), 1–4.
- (76) Blaschke, B. M.; Lottner, M.; Drieschner, S.; Calia, A. B.; Stoiber, K.; Rousseau, L.; Lissourges, G.; Garrido, J. A. Flexible Graphene Transistors for Recording Cell Action Potentials. *2D Mater.* **2016**, *3* (2), 025007.
- (77) Kireev, D.; Brambach, M.; Seyock, S.; Maybeck, V.; Fu, W.; Wolfrum, B.; Offenhäusser, A. Graphene Transistors for Interfacing with Cells: Towards a Deeper Understanding of Liquid Gating and Sensitivity. *Sci. Rep.* **2017**, *7* (1), 6658.
- (78) Schottdorf, M.; Hofmann, B.; Kästelhön, E.; Offenhäusser, A.; Wolfrum, B. Frequency-Dependent Signal Transfer at the Interface between Electrogenic Cells and Nanocavity Electrodes. *Phys. Rev. E - Stat. Nonlinear, Soft Matter Phys.* **2012**, *85* (3), 1–7.
- (79) Nelea, V.; Nakano, Y.; Kaartinen, M. T. Size Distribution and Molecular Associations of Plasma Fibronectin and Fibronectin Crosslinked by Transglutaminase 2. *M.T. Protein J* **2008**, *27*:223.

Erklärung

Ich versichere, dass ich die von mir vorgelegte Dissertation selbständig angefertigt, die benutzten Quellen und Hilfsmittel vollständig angegeben und die Stellen der Arbeit – einschließlich Tabellen, Karten und Abbildungen –, die anderen Werken im Wortlaut oder dem Sinn nach entnommen sind, in jedem Einzelfall als Entlehnung kenntlich gemacht habe; dass diese Dissertation noch keiner anderen Fakultät oder Universität zur Prüfung vorgelegen hat; dass sie – abgesehen von unten angegebenen Teilpublikationen – noch nicht veröffentlicht worden ist sowie, dass ich eine solche Veröffentlichung vor Abschluss des Promotionsverfahrens nicht vornehmen werde.

Die Bestimmungen dieser Promotionsordnung sind mir bekannt. Die von mir vorgelegte Dissertation ist von Prof. Dr. Roger Wördenweber betreut worden.

Teilpublikationen liegen vor:

1. Markov, A., Wolf, N., Yuan, X., Mayer, D., Maybeck, V, Offenhäusser, A and Wördenweber, R. Controlled Engineering of Oxide Surfaces for Bioelectronics Applications Using Organic Mixed Monolayers // ACS Appl. Mater. Interfaces 2017 DOI: 10.1021/acsami.7b08481
2. Markov, A.; Greben, K.; Mayer, D.; Offenhäusser, A.; Wördenweber, R. In Situ Analysis of the Growth and Dielectric Properties of Organic Self-Assembled Monolayers: A Way To Tailor Organic Layers for Electronic Applications. // ACS Appl. Mater. Interfaces 2016, 8 (25), 16451–16456 DOI: 10.1021/acsami.6b04021

Ich versichere, dass ich alle Angaben wahrheitsgemäß nach bestem Wissen und Gewissen gemacht habe und verpflichte mich, jedmögliche, die obigen Angaben betreffenden Veränderungen, dem Dekanat unverzüglich mitzuteilen.

Datum 22.01.2017

Unterschrift



Lebenslauf



Name: **Aleksandr Markov**
Date of birth: 19.06.1990
Place of birth: Jambul, Kazakhstan
Marital status: Married
Citizenship: Russian
Address: Friedrich-Ebert-Str. 31, 52428 Jülich, NRW
Germany

2014-2017 PhD Student in Physics

Title: "Tailoring and characterization of bioelectronics interfaces"

Place: Peter Grünberg Institute (PGI-8) / Institute of Complex Systems (ICS-8) Forschungszentrum Jülich (FZJ), Germany. Under supervision of Prof. Dr. Roger Würdenweber and Prof. Dr. Andreas Offenhäusser.

2012-2014 Master of Science degree at St.-Petersburg State Electrotechnical University

Title: "Technological aspects of the fabrication of multilayer thin-film structures for microwave application"

Place: Peter Grünberg Institute, Forschungszentrum Jülich (FZJ), Germany /
Electronics faculty of St.-Petersburg State Electrotechnical University, Russia

2008-2012 Bachelor of Science degree at St.-Petersburg State Electrotechnical University

Title: "Research of capacitive elements on the base of BSTO thin films"

Place: Electronics faculty of St.-Petersburg State Electrotechnical University, Russia

Band / Volume 149

Kinetic and thermodynamic considerations on the formation of heteromolecular layers on metal surfaces

C. Henneke (2017), vii, 157, XIV pp

ISBN: 978-3-95806-245-0

Band / Volume 150

Spectroscopic characterization of local valence change processes in resistively switching complex oxides

C. Bäumer (2017), x, 206 pp

ISBN: 978-3-95806-246-7

Band / Volume 151

Magnetic structure in relation to the magnetic field induced ferroelectricity in Y-type hexaferrite $\text{Ba}_{2-x}\text{Sr}_x\text{Zn}_2\text{Fe}_{12}\text{O}_{22}$

P. Thakuria (2017), 17, 180 pp

ISBN: 978-3-95806-250-4

Band / Volume 152

Statistical analysis tools for assessing the functional relevance of higher-order correlations in massively parallel spike trains

V. Rostami (2017), x, 176 pp

ISBN: 978-3-95806-251-1

Band / Volume 153

The influence of the substrate on the structure and electronic properties of carbon-based 2D materials

J. Sforzini (2017), XIII, 145 pp

ISBN: 978-3-95806-255-9

Band / Volume 154

Gate-All-Around Silicon Nanowire Tunnel FETs for Low Power Applications

G. V. Luong (2017), ii, 136 pp

ISBN: 978-3-95806-259-7

Band / Volume 155

Graphene Devices for Extracellular Measurements

D. Kireev (2017), ix, 169 pp

ISBN: 978-3-95806-265-8

Band / Volume 156

Nanoscale 3D structures towards improved cell-chip coupling on microelectrode arrays

S. D. Weidlich (2017), II, 154 pp

ISBN: 978-3-95806-278-8

Band / Volume 157

Interface phenomena in $\text{La}_{1/3}\text{Sr}_{2/3}\text{FeO}_3$ / $\text{La}_{2/3}\text{Sr}_{1/3}\text{MnO}_3$ heterostructures and a quest for p-electron magnetism

M. Waschk (2017), ix, 205 pp

ISBN: 978-3-95806-281-8

Band / Volume 158

Physics of Life

Lecture Notes of the 49th IFF Spring School 2018

26 February – 09 March 2018, Jülich, Germany

ed. by G. Gompfer, J. Dhont, J. Elgeti, C. Fahlke, D. Fedosov,

S. Förster, P. Lettinga, A. Offenhäusser (2018), ca 1000 pp

ISBN: 978-3-95806-286-3

Band / Volume 159

Identifizierung von Bindungsdeterminanten von Tat-Vorläuferproteinen an den TatBCRezeptorkomplex während der Tat-abhängigen Proteintranslokation in *Escherichia coli*

A. Ulfing (2018), 186 pp

ISBN: 978-3-95806-290-0

Band / Volume 160

***Corynebacterium glutamicum* – a novel platform for the production of plant polyphenols**

N. Kallscheuer (2018), XIII, 98 pp

ISBN: 978-3-95806-291-7

Band / Volume 161

Neurons on 3D polymer nanostructures

A. Belu (2018), vii, 135 pp

ISBN: 978-3-95806-296-2

Band / Volume 162

Tailoring and Characterisation of Bioelectronic Interfaces

A. Markov (2018), 75 pp

ISBN: 978-3-95806-298-6

Weitere **Schriften des Verlags im Forschungszentrum Jülich** unter
<http://www.zwb1.fz-juelich.de/verlagextern1/index.asp>

Schlüsseltechnologien / Key Technologies

Band / Volume 162

ISBN 978-3-95806-298-6